



ALMA ACA and Nobeyama Observations of Two Orion Cores in Deuterated Molecular Lines

Ken'ichi Tatematsu^{1,2} , Tie Liu^{3,4,5} , Gwanjeong Kim¹ , Hee-Weon Yi⁶ , Jeong-Eun Lee⁶ , Naomi Hirano⁷ , Sheng-Yuan Liu⁷ , Satoshi Ohashi⁸ , Patricio Sanhueza^{2,9} , James Di Francesco^{10,11} , Neal J. Evans II¹² , Gary A. Fuller¹³ , Ryo Kandori⁹ , Minhoo Choi⁴ , Miju Kang⁴ , Siyi Feng^{9,14} , Tomoya Hirota^{2,9} , Takeshi Sakai¹⁵ , Xing Lu⁹ , Quang Nguyễn Lu'o'ng^{4,9,16,17} , Mark A. Thompson¹⁸ , Yuefang Wu¹⁹ , Di Li²⁰ , Kee-Tae Kim^{4,25} , Ke Wang^{14,21} , Isabelle Ristorcelli²² , Mika Juvela²³ , and L. Viktor Tóth²⁴ 

¹ Nobeyama Radio Observatory, National Astronomical Observatory of Japan, National Institutes of Natural Sciences, 462-2 Nobeyama, Minamimaki, Minamisaku, Nagano 384-1305, Japan; k.tatematsu@nao.ac.jp

² Department of Astronomical Science, SOKENDAI (The Graduate University for Advanced Studies), 2-21-1 Osawa, Mitaka, Tokyo 181-8588, Japan

³ Key Laboratory for Research in Galaxies and Cosmology, Shanghai Astronomical Observatory, Chinese Academy of Sciences, 80 Nandan Road, Shanghai 200030, People's Republic of China

⁴ Korea Astronomy and Space Science Institute, Daedeokdaero 776, Yuseong, Daejeon 305-348, Republic of Korea

⁵ East Asian Observatory, 660 N. A'ohoku Place, Hilo, HI 96720, USA

⁶ School of Space Research, Kyung Hee University, Seocheon-Dong, Giheung-Gu, Yongin-Si, Gyeonggi-Do, 446-701, Republic of Korea

⁷ Academia Sinica Institute of Astronomy and Astrophysics, 11F of Astronomy-Mathematics Building, AS/NTU, No.1, Sec. 4, Roosevelt Rd, Taipei 10617, Taiwan, R.O.C.

⁸ The Institute of Physical and Chemical Research (RIKEN), 2-1, Hirosawa, Wako-shi, Saitama 351-0198, Japan

⁹ National Astronomical Observatory of Japan, National Institutes of Natural Sciences, 2-21-1 Osawa, Mitaka, Tokyo 181-8588, Japan

¹⁰ Herzberg Astronomy & Astrophysics, National Research Council of Canada, 5071 West Saanich Road, Victoria, BC V9E 2E7, Canada

¹¹ Department of Physics and Astronomy, University of Victoria, Victoria, BC V8W 2Y2, Canada

¹² Department of Astronomy, The University of Texas at Austin, 2515 Speedway, Stop C1400, Austin, TX 78712–1205, USA

¹³ Jodrell Bank Centre for Astrophysics, School of Physics and Astronomy, University of Manchester, Oxford Road, Manchester, M13 9PL, UK

¹⁴ The Kavli Institute for Astronomy and Astrophysics, Peking University, 5 Yiheyuan Road, Haidian District, Beijing 100871, People's Republic of China

¹⁵ Graduate School of Informatics and Engineering, The University of Electro-Communications, Chofu, Tokyo 182-8585, Japan

¹⁶ McMaster University, 1 James Street North, Hamilton, ON, L8P 1A2, Canada

¹⁷ IBM, Canada

¹⁸ Centre for Astrophysics Research, Science & Technology Research Institute, University of Hertfordshire, Hatfield, AL10 9AB, UK

¹⁹ Department of Astronomy, Peking University, 100871, Beijing, People's Republic of China

²⁰ National Astronomical Observatories, Chinese Academy of Sciences, Beijing, 100012, People's Republic of China

²¹ European Southern Observatory, Karl-Schwarzschild-Str. 2 D-85748 Garching bei München, Germany

²² RAP, CNRS (UMR5277), Université Paul Sabatier, 9 avenue du Colonel Roche, BP 44346, F-31028, Toulouse Cedex 4, France

²³ Department of Physics, P.O. Box 64, FI-00014, University of Helsinki, Finland

²⁴ Department of Astronomy, Eötvös Loránd University, Pázmány Péter sétány 1/A, H-1117 Budapest, Hungary

²⁵ University of Science and Technology, Korea (UST), 217 Gajeong-ro, Yuseong-gu, Daejeon 34113, Republic of Korea

Received 2020 March 25; revised 2020 April 21; accepted 2020 April 23; published 2020 June 3

Abstract

We mapped two molecular cloud cores in the Orion A cloud with the 7 m Array of the Atacama Compact Array (ACA) of the Atacama Large Millimeter/submillimeter Array (ALMA) and with the Nobeyama 45 m radio telescope. These cores have bright N_2D^+ emission in single-pointing observations with the Nobeyama 45 m radio telescope, have a relatively high deuterium fraction, and are thought to be close to the onset of star formation. One is a star-forming core, and the other is starless. These cores are located along filaments observed in N_2H^+ and show narrow line widths of 0.41 km s^{-1} and 0.45 km s^{-1} in N_2D^+ , respectively, with the Nobeyama 45 m telescope. Both cores were detected with the ALMA ACA 7 m Array in the continuum and molecular lines at Band 6. The starless core G211 shows a clumpy structure with several sub-cores, which in turn show chemical differences. Also, the sub-cores in G211 have internal motions that are almost purely thermal. The starless sub-core G211D, in particular, shows a hint of the inverse P Cygni profile, suggesting infall motion. The star-forming core G210 shows an interesting spatial feature of two N_2D^+ peaks of similar intensity and radial velocity located symmetrically with respect to the single dust continuum peak. One interpretation is that the two N_2D^+ peaks represent an edge-on pseudo-disk. The CO outflow lobes, however, are not directed perpendicular to the line connecting both N_2D^+ peaks.

Unified Astronomy Thesaurus concepts: [Star forming regions \(1565\)](#); [Astrochemistry \(75\)](#); [Interstellar medium \(847\)](#); [Giant molecular clouds \(653\)](#); [Molecular clouds \(1072\)](#); [Collapsing clouds \(267\)](#)

1. Introduction

Understanding initial conditions is essential for star formation studies. The molecular cloud core is the densest part of the hierarchical structure of the interstellar medium. Although there are numerous molecular cloud cores, only a small proportion are likely close to the onset of star formation. Different initial conditions probably lead to different star formation modes.

Therefore, we need to have good examples in different environments (low-mass star formation in less-turbulent “nearby dark clouds” versus high-mass star formation in more turbulent “giant molecular clouds” (GMCs)). L1544 has served as a very interesting starless core showing gravitational collapse in nearby dark clouds (Tafalla et al. 1998; Caselli et al. 2019; Redaelli et al. 2019) that is on the verge of star

Table 1
Molecular Lines Observed with the Nobeyama 45 m Radio Telescope

Line	Frequency (GHz)	rms Noise Level ^a (K)
CCS ($J_N = 7_6-6_5$)	81.505208	0.10
CCS ($J_N = 8_7-7_6$)	93.870107	0.10
HC ₃ N ($J = 9-8$)	81.8814614	0.09
N ₂ H ⁺ ($J = 1-0$)	93.1737767	0.12
DNC ($J = 1-0$)	76.3057270	0.09
HN ¹³ C ($J = 1-0$)	87.090859	0.09
N ₂ D ⁺ ($J = 1-0$)	77.1096100	0.07
cyclic C ₃ H ₂ ($J_{K_a K_c} = 2_{12}-1_{01}$)	85.338906	0.09

Note.

^a At the spectrometer resolution.

formation. Because the majority of stars form in GMCs rather than dark clouds, however, understanding star formation in GMCs is of great importance. Studies in infrared dark clouds (IRDCs), which are dense parts of GMCs, have been extensively made (Sanhueza et al. 2012, 2019; Feng et al. 2016; Contreras et al. 2018; Lu et al. 2018; Chen et al. 2019), while the importance of the nearest, archetypal GMC, Orion A, remains because of its proximity. According to Blitz (1990), the global properties of GMCs are: masses of $(1 - 2) \times 10^5 \mathcal{M}_\odot$, mean diameters of 45 pc, and mean average H₂ column densities of $(3-6) \times 10^{21} \text{ cm}^{-2}$. IRDCs are clumps inside GMCs with temperatures 10–25 K, sizes of 1–10 pc, H₂ densities of $\sim 10^6 \text{ cm}^{-3}$, and H₂ column densities up to $\sim 10^{23} \text{ cm}^{-2}$ (P  rault et al. 1996; Carey et al. 2000).

It is not clear yet how stars start to form. Most observed molecular cloud cores seem to be in stable equilibrium or have evolutionary timescales much longer than the free-fall timescale, at least in low-mass star-forming regions (Myers et al. 1983; Onishi et al. 2002). Furthermore, molecular cloud cores should be marginally magnetically supercritical in theory (Nakano 1998) and seem so observationally (Crutcher 2012). On the other hand, if molecular cloud cores are formed in a nonequilibrium stable state or unstable state (even including magnetic contributions), they will evolve very quickly; namely, the timescale to form stars is not much longer than the free-fall time. Given that observed starless cores are in dynamical equilibrium and stable, there should be a mechanism to change a stable core into an unstable one.

N₂D⁺ is one of the most important molecules, as it allows us to investigate the densest regions of molecular cloud cores (Kong et al. 2017; Salinas et al. 2017; Aikawa et al. 2018; Murillo et al. 2018; Punanova et al. 2018; van ’t Hoff et al. 2018; Riaz et al. 2019; Tobin et al. 2019; Tokuda et al. 2019). N₂H⁺ is known to be a molecule weakly affected by depletion in cold, dense regions (Bergin et al. 2002). N₂D⁺ seems to be even less affected by depletion than N₂H⁺ (Pagani et al. 2007). Furthermore, the deuterium fraction of some molecular species such as N₂D⁺ increases in the starless phase (Crapsi et al. 2005; Fontani et al. 2006; Emprechtinger et al. 2009) and then decreases after the onset of star formation (Sakai et al. 2012; De Simone et al. 2018; Stephens et al. 2018). Therefore, molecular cloud cores with high deuterium fractions of N₂D⁺ are most likely to be close to the onset of star formation. By using the protostellar data and the N₂D⁺ data, we can categorize cores not only “before” and “after” star formation but also evaluate evolutionary stages in them such as “early starless”, “late starless” (closer to the onset of star formation), “early protostellar”, and “late protostellar.” In this

Table 2
Molecular Lines Observed with the ACA

Line	Frequency (GHz)
DCO ⁺ ($J = 3-2$)	216.112580
DCN ($J = 3-2$)	217.238530
DNC ($J = 3-2$)	228.910490 ^a
CO ($J = 2-1$)	230.538000
N ₂ D ⁺ ($J = 3-2$)	231.321828
CS ($J = 5-4$)	244.935556
H ¹³ CN ($J = 3-2$)	259.011787
H ¹³ CO ⁺ ($J = 3-2$)	260.255342
HCN ($J = 3-2$)	265.886431
HCO ⁺ ($J = 3-2$)	267.557633

Note.

^a This should be 228.910489, but the difference is negligible for the purposes of this study.

paper, we adopted the catalog of Yi et al. (2018) and regard a core as starless if it is not associated with a protostar.

2. Observations

2.1. Source Selection

To find the best examples of molecular cloud cores with high deuterium fractions in GMCs, we conducted an astrochemical census toward the Orion region. First, we performed an extensive study based on 850 μm observations with the SCUBA-2 camera on board the James Clerk Maxwell telescope (JCMT) toward the Planck Galactic Cold Clumps (PGCCs; 10–20 K) for the JCMT Legacy program “SCOPE”²⁶ (SCUBA-2 Continuum Observations of Pre-protostellar Evolution, PI = Tie Liu; Liu et al. 2018). Based on the Planck all-sky survey data (Planck Collaboration XXIII 2011; Planck Collaboration XXVIII 2016), we also carried out a series of line observations of molecular clouds with ground-based radio telescopes for the TOP-SCOPE Planck Cold Clump collaboration to understand the initial condition for star formation. For example, “TOP”²⁷ (TRAO Observations of Planck cold clump, PI Tie Liu) is a related Key Science Program with the TRAO 14 m radio telescope. To minimize the distance uncertainty, we selected the Orion star-forming region for this study. For the Orion region, we cataloged 119 SCUBA-2 cores in PGCCs (Yi et al. 2018). Then, we observed these cores with the Nobeyama 45 m telescope in the $J = 1-0$ transitions of N₂H⁺, N₂D⁺, DNC, HN¹³C, and other lines (Kim et al. 2020). From these, we selected two cores bright in N₂D⁺ emission. One is a star-forming core (G210.82–19.47 North1; here, we call it G210), and the other is a starless core (G211.16–19.33 North3; here, we call it G211). G210 includes the Herschel source HOPS 157 (Furlan et al. 2016), which is classified as a Class I young stellar object. Its bolometric luminosity and bolometric temperature are $L_{\text{bol}} = 3.8 \mathcal{L}_\odot^{\text{N}}$ and $T_{\text{bol}} = 77.6 \text{ K}$, respectively. This bolometric temperature is close to the boundary value of 70 K between Class 0 and Class I (Chen et al. 1995). The best-fit envelope mass within 2500 au ($6''$) is $0.4 \mathcal{M}_\odot^{\text{N}}$. However, Yi et al. (2018) derived a bolometric luminosity and bolometric temperature of $L_{\text{bol}} = 1.1 \mathcal{L}_\odot^{\text{N}}$ and $T_{\text{bol}} = 213 \text{ K}$, respectively.

²⁶ <https://www.eaobservatory.org/jcmt/science/large-programs/scope/>

²⁷ http://radio.kasi.re.kr/trao/key_science.php

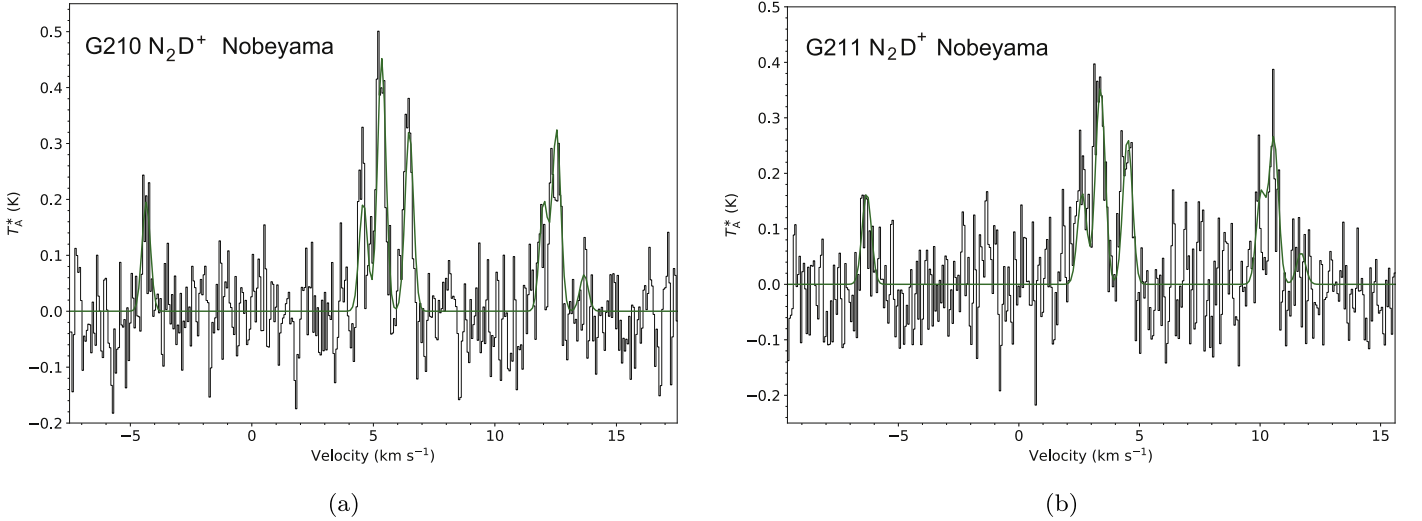


Figure 1. N_2D^+ spectra (black lines) obtained toward G210 and G211 with the Nobeyama 45 m radio telescope and hyperfine fitting results (smooth green curves). Panel (a): G210; panel (b): G211.

Table 3
Line Parameters from Observations with the Nobeyama 45 m Telescope

Source	Line	T_A^* (K)	V_{LSR} (km s $^{-1}$)	Δv^a (km s $^{-1}$)	$T_{ex} * \tau(\text{main})^b$ (K)	$\tau(\text{main})$
G210	82 GHz CCS ($J_N = 7_6-6_5$)	<0.18
	94 GHz CCS ($J_N = 8_7-6_5$)	<0.19
	HC $_3$ N ($J = 9-8$)	<0.22
	c-C $_3$ H $_2$ ($J_{KaKc} = 2_{12}-1_{01}$)	0.47	5.31	0.76
	DNC ($J = 1-0$)	0.82	5.43	0.98
	HN 13 C ($J = 1-0$)	0.21	5.47	1.12
	N_2D^+ ($J = 1-0$)	0.45	5.34	0.41	3.4 ± 0.2	0.4 ± 0.1
	N_2H^+ ($J = 1-0$)	1.30	5.30	0.44	13.5 ± 0.9	2.7 ± 0.7
G211	82 GHz CCS ($J_N = 7_6-6_5$)	0.18	3.28	0.40
	94 GHz CCS ($J_N = 8_7-6_5$)	<0.15
	HC $_3$ N ($J = 9-8$)	0.70	3.39	0.39
	c-C $_3$ H $_2$ ($J_{KaKc} = 2_{12}-1_{01}$)	1.34	3.25	0.43
	DNC ($J = 1-0$)	0.96	3.48	1.09
	HN 13 C ($J = 1-0$)	0.46	3.36	0.68
	N_2D^+ ($J = 1-0$)	0.37	3.38	0.45	3.0 ± 0.6	1.1 ± 1.1
	N_2H^+ ($J = 1-0$)	1.03	3.33	0.35	19.5 ± 1.4	9.9 ± 1.2

Notes. The error of the line intensity is about 10%. The errors of the LSR velocity and line width are less than 0.1 km s $^{-1}$.

^a The DNC and HN 13 C line widths are overestimated, because we ignore hyperfine splitting.

^b The optical depth of the main (brightest) hyperfine component.

Yi et al. (2018) mainly used Wide-field Infrared Survey Explorer (WISE) data points and missed the mid-infrared ranges, which can cause overestimation of T_{bol} . The spectral indices of HOPS 157 are 1.74 (Furlan et al. 2016) and 1.22 (Yi et al. 2018), both of which suggest that the source is Class I. Both G210 and G211 belong to the dark cloud L1641 (Lynds 1962) of the Orion A GMC (Maddalena et al. 1986), but outside the Orion Nebula region, and are close to each other in the sky ($22' = 3$ pc apart). Given their proximity, they may be cores caught before and after the onset of star formation in *similar environments*. Furthermore, they are located along the $^{13}\text{CO } J=1-0$ filaments observed by Nagahama et al. (1998). G210 is located at the northern tip of filament #24, and G211 is located at the intersection of two filaments, #26 and #28. By comparing these SCUBA-2 cores with CS cores cataloged in previous observations, we found the following coincidences. The CS ($J=2-1$) core FC-24 (Tatematsu et al. 1998)

corresponds to a combination of G210.82–19.47 North1 (G210) and North2. Meanwhile, the CS ($J=1-0$) core TUKH101 cataloged in Tatematsu et al. (1993) corresponds to G211. We will discuss the physical parameters of these single-dish CS cores later.

A distance to the Orion A GMC of 398 ± 7 pc from Getman et al. (2019) is adopted for this paper.

2.2. Nobeyama 45 m Radio Telescope

Observations with the 45 m radio telescope of the Nobeyama Radio Observatory²⁸ were performed in 2017 February, 2018 January, and 2018 February (proposal IDs: CG161004, LP177001). We observed eight molecular lines, CCS

²⁸ Nobeyama Radio Observatory is a branch of the National Astronomical Observatory of Japan, National Institutes of Natural Sciences.

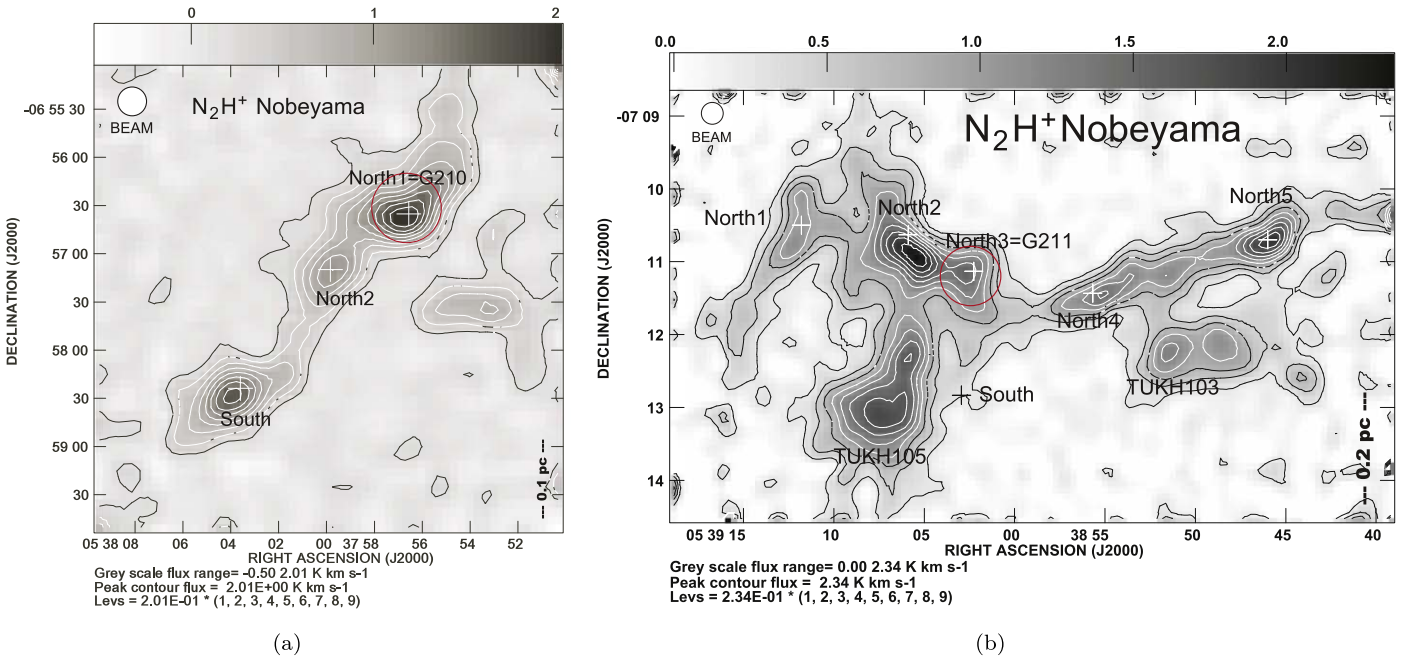


Figure 2. The integrated intensity map of $\text{N}_2\text{H}^+ J = 1-0$ toward the G210.82–19.47 region including G210 and the G211.16–19.33 region including G211 obtained with the Nobeyama 45 m telescope. The emission is integrated for the main hyperfine component group $J = 1 \rightarrow 0 F_1 = 2 \rightarrow 1$ consisting of three components, including the most intense one. The plus signs represent the locations of SCUBA-2 peak positions. The red circle represents the field of view (50% level) of the corresponding ACA observations.

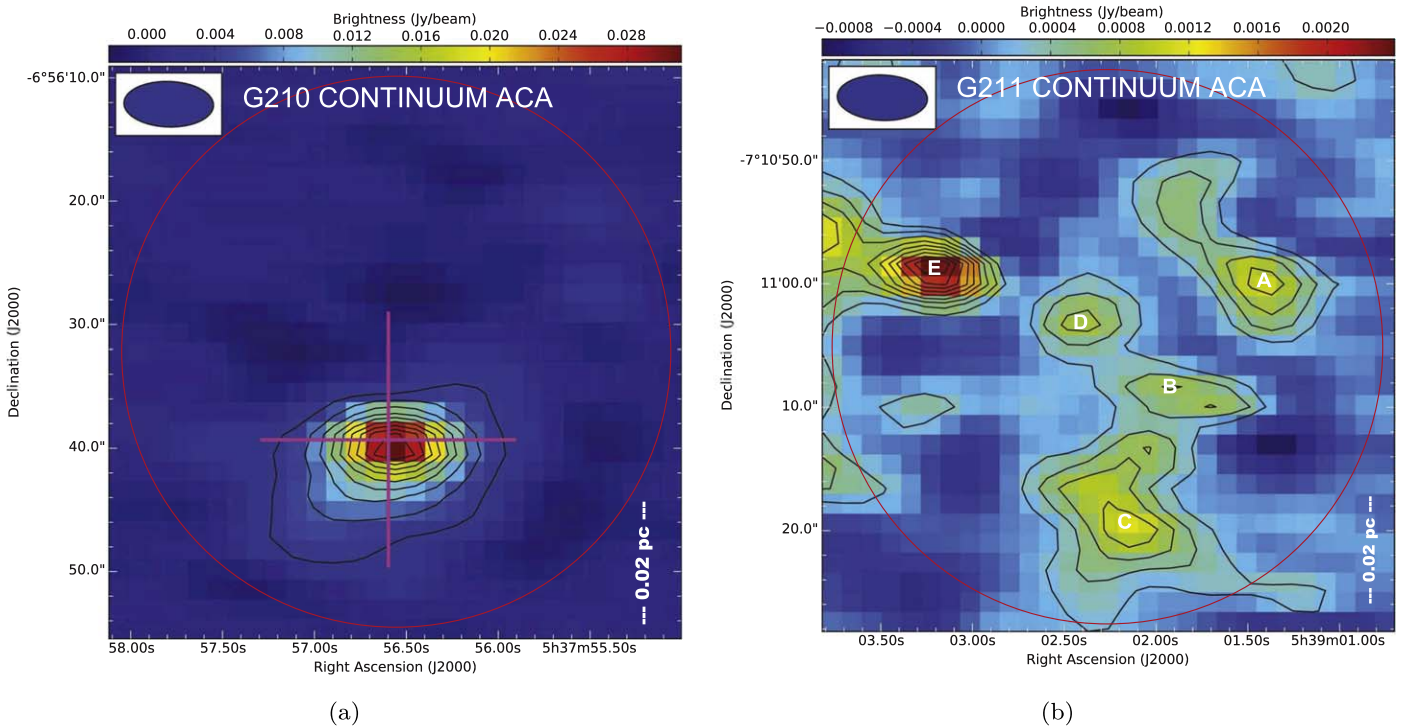


Figure 3. The 1.2 mm continuum map toward G210 and G211. Contour levels are shown in steps of 10% of the maximum value. The cross symbol represents the continuum peak position of G210. Local peaks in G211 are designated A through E. The ellipse in the top-left corner represents the half-intensity synthesized beam size. The red circle illustrates the field of view (50% level) of the ACA observations.

$J_N = 7_6-6_5$ and $J_N = 8_7-7_6$, $\text{HC}_3\text{N } J = 9-8$, $\text{N}_2\text{H}^+ J = 1-0$, $\text{HN}^{13}\text{C } J = 1-0$, $\text{DNC } J = 1-0$, $\text{N}_2\text{D}^+ J = 1-0$, and 85 GHz cyclic $\text{C}_3\text{H}_2 J_{\text{KaKc}} = 2_{12}-1_{02}$ by using the receivers TZ1 (Asayama & Nakajima 2013; Nakajima et al. 2013), T70, and FOREST (Minamidani et al. 2016). The employed line frequencies are summarized in Table 1. Please

refer to Tatematsu et al. (2017) for references for frequencies. The employed receiver backend was the SAM45 digital spectrometer (Kamazaki et al. 2012).

The FWHM beam sizes at 86 GHz with TZ1 and T70 were $18''.2 \pm 0''.1$ and $18''.9 \pm 0''.4$, respectively. The main-beam efficiency η_{mb} at 86 GHz with TZ1 was $54 \pm 3\%$. The value of

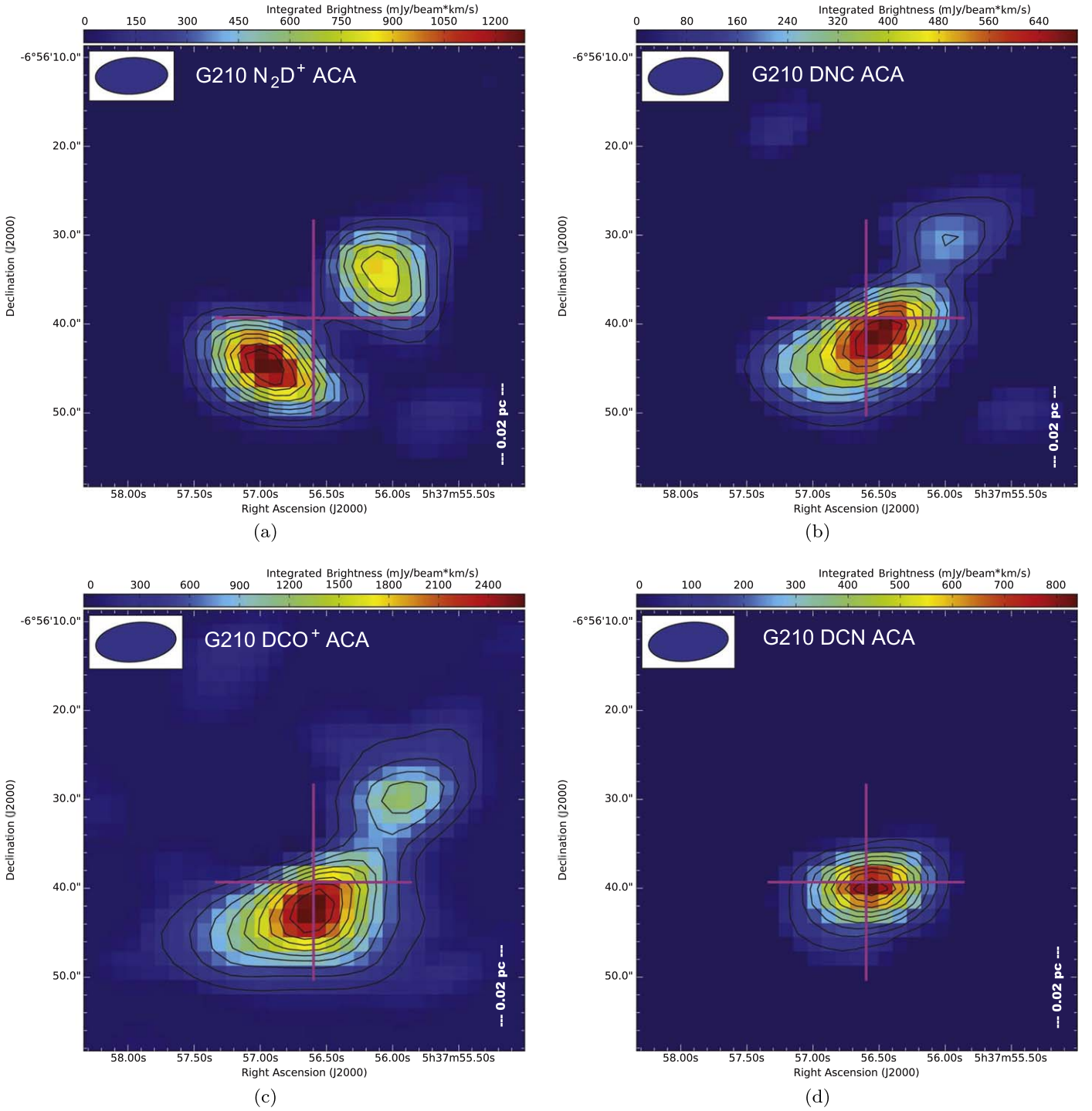


Figure 4. The velocity-integrated intensity maps of G210 are shown as follows: panel (a): N₂D⁺ $J = 3-2$ ($V_{\text{LSR}} = 4.57-5.94 \text{ km s}^{-1}$); panel (b): DNC $J = 3-2$ ($V_{\text{LSR}} = 4.81-5.75 \text{ km s}^{-1}$); panel (c) DCO⁺ $J = 3-2$ ($V_{\text{LSR}} = 4.59 \text{ to } 6.00 \text{ km s}^{-1}$); and panel (d) DCN $J = 3-2$ ($V_{\text{LSR}} = 4.81-6.11 \text{ km s}^{-1}$). The N₂D⁺ emission is integrated for the main hyperfine component group including the brightest one. 1 mJy beam⁻¹ corresponds to 0.69 mK, 0.67 mK, 0.66 mK, and 0.67 mK for panels (a), (b), (c), and (d), respectively.

η_{mb} with T70 was $43 \pm 4\%$. The FWHM beam size at 86 GHz with FOREST was $19''.0 \pm 0''.5$. The value of η_{mb} at 86 GHz with FOREST was $56 \pm 5\%$. The spectral resolution was 15.26 kHz (corresponding to $0.05-0.06 \text{ km s}^{-1}$) for both the TZ1 and T70 observations. The spectral resolution of the FOREST observations, however, was set to a value twice as large,

30.52 kHz (corresponding to $0.10-0.12 \text{ km s}^{-1}$), unintentionally. Single-pointing observations with TZ1 and T70 (partly with FOREST) were performed in the ON-OFF position-switching mode. Mapping observations with FOREST were made in the on-the-fly mapping mode (Sawada et al. 2008). The map sizes are a $5'$ square and $12' \times 6'$ for G210 and G211, respectively.

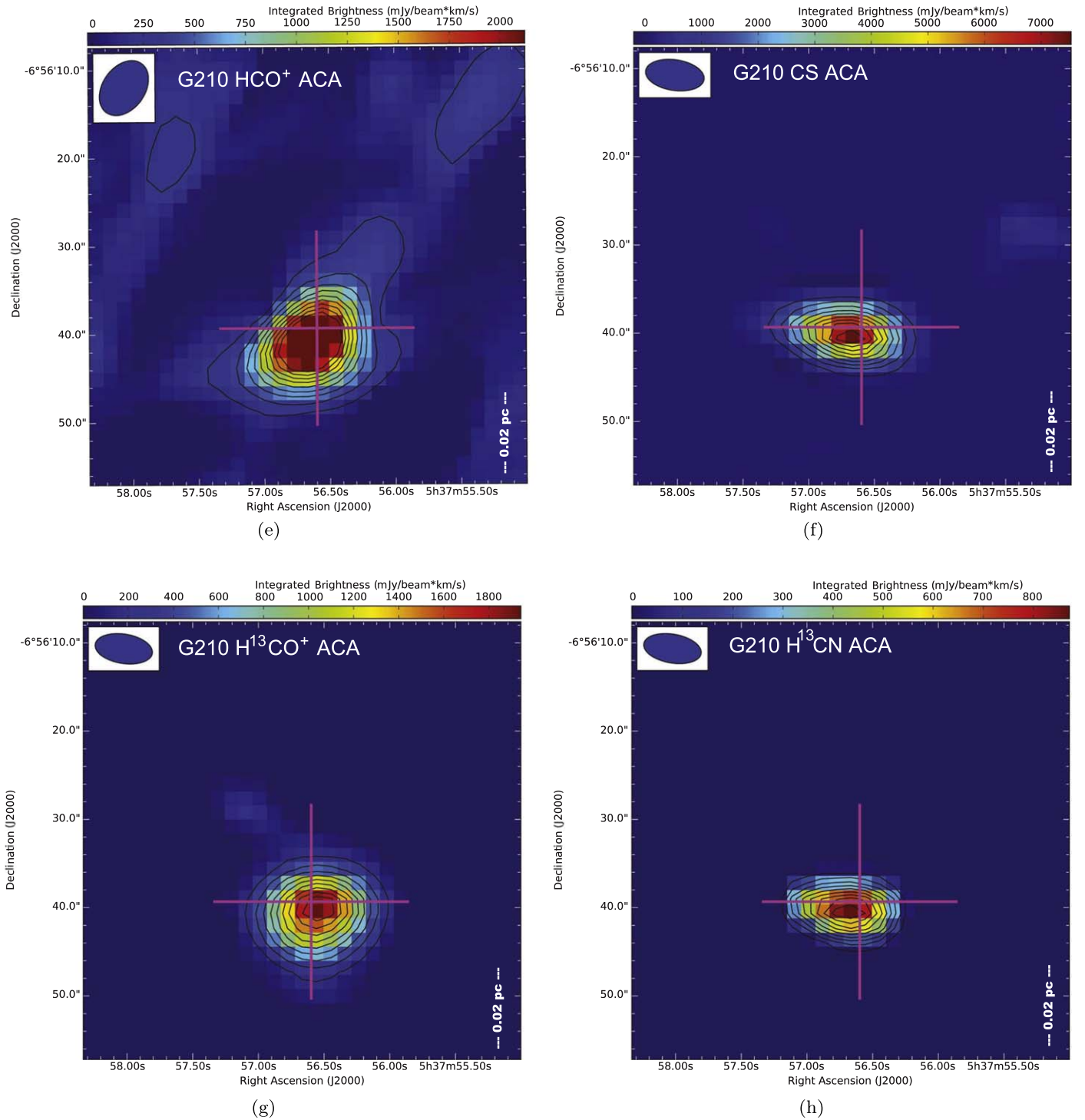


Figure 5. Information presented here is similar to that in Figure 4, showing the velocity-integrated intensity maps of G210 as follows: panel (e) $\text{HCO}^+ J = 3-2$ ($V_{\text{LSR}} = 4.94-5.41 \text{ km s}^{-1}$); panel (f): $\text{CS } J = 5-4$ ($V_{\text{LSR}} = 3.71-5.53 \text{ km s}^{-1}$); panel (g): $\text{H}^{13}\text{CO}^+ J = 3-2$ ($V_{\text{LSR}} = 4.60-6.03 \text{ km s}^{-1}$); and panel (h): $\text{H}^{13}\text{CN } J = 3-2$ ($V_{\text{LSR}} = 4.67-6.72 \text{ km s}^{-1}$). 1 mJy beam^{-1} corresponds to 0.52, 0.88, 0.83, and 0.85 mK for panels (e), (f), (g), and (h), respectively.

The observed intensity is reported in terms of the corrected antenna temperature T_A^* . The main-beam radiation temperature can be derived as $T_{\text{mb}} = T_A^*/\eta_{\text{mb}}$. The telescope pointing was established by observing relevant 43 GHz SiO maser sources every ~ 60 minutes and was accurate to $\sim 5''$. The observed data were reduced using the software packages “NewStar” and “NoStar” of the Nobeyama Radio Observatory, for single-pointing and on-the-fly observations, respectively.

2.3. ALMA ACA 7 m Array

We observed the two selected cores using the 7 m Array of the Atacama Compact Array (ACA; a.k.a, the Morita Array; Iguchi et al. 2009), which is a part of the Atacama Large Millimeter/submillimeter Array (ALMA). Observations were made on 2017 July 13, 2017 August 19, and 2017 August 24 as a 7 m Supplemental Call program of ALMA Cycle 4 (proposal ID: 2016.2.00058.S). The ALMA Band 6 receivers were used

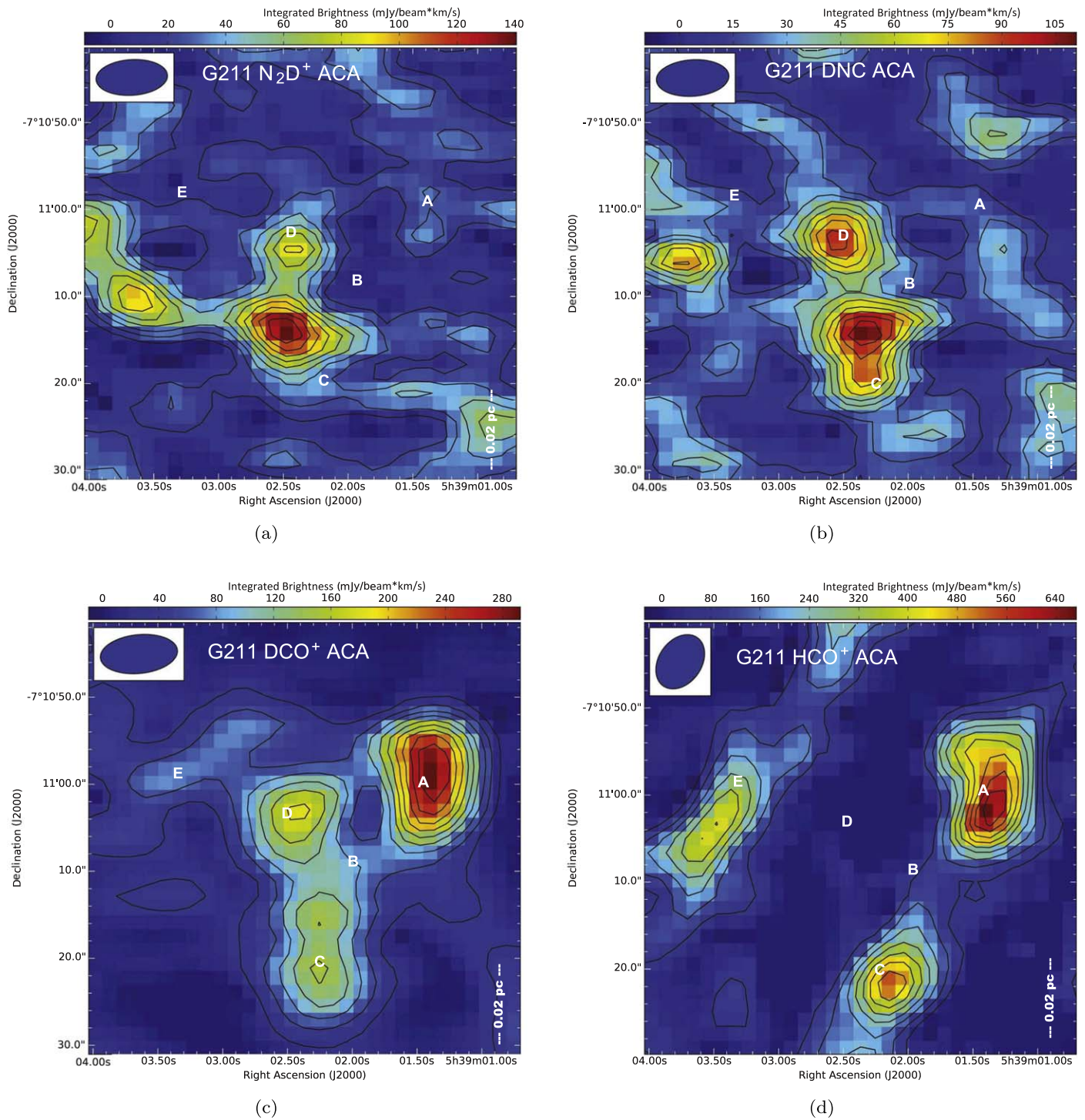


Figure 6. Information presented here is similar to that in Figure 4 and includes the velocity-integrated intensity maps of G211 as follows: panel (a): N_2D^+ $J = 3-2$ ($V_{LSR} = 2.86-4.18$ km s $^{-1}$); panel (b): DNC $J = 3-2$ ($V_{LSR} = 3.03-4.02$ km s $^{-1}$); panel (c): DCO^+ $J = 3-2$ ($V_{LSR} = 3.13-3.81$ km s $^{-1}$); and panel (d): HCO^+ $J = 3-2$ ($V_{LSR} = 3.36-3.83$ km s $^{-1}$). 1 mJy beam $^{-1}$ corresponds to 0.68, 0.67, 0.67, and 0.52 mK for panels (a), (b), (c), and (d), respectively. The continuum peak positions are labeled.

to image the molecular lines listed in Table 2 as well as the 1.2 mm continuum emission. Rest frequencies were taken from Splatalogue entries²⁹ adopted in the ALMA Observing Tool³⁰ except for DNC and $HN^{13}C$, whose frequencies are not listed in this catalog. Instead, the rest frequencies for DNC and $HN^{13}C$

²⁹ <https://www.cv.nrao.edu/php/splatalogue/>

³⁰ almascience.org

were taken from the JPL Catalog (Pickett et al. 1998). The spectral resolution was 122.1 kHz (corresponding to 0.14–0.17 km s $^{-1}$) for the line emission. The mosaic observations consist of three telescope pointings. The bandpass and secondary flux calibrator were J0522-3627, and the phase calibrator was J0501-0159 or J0542-0913. G210 and G211 were observed with the phase calibrator in a repeated cycle, and they should have the same calibration quality. The number of

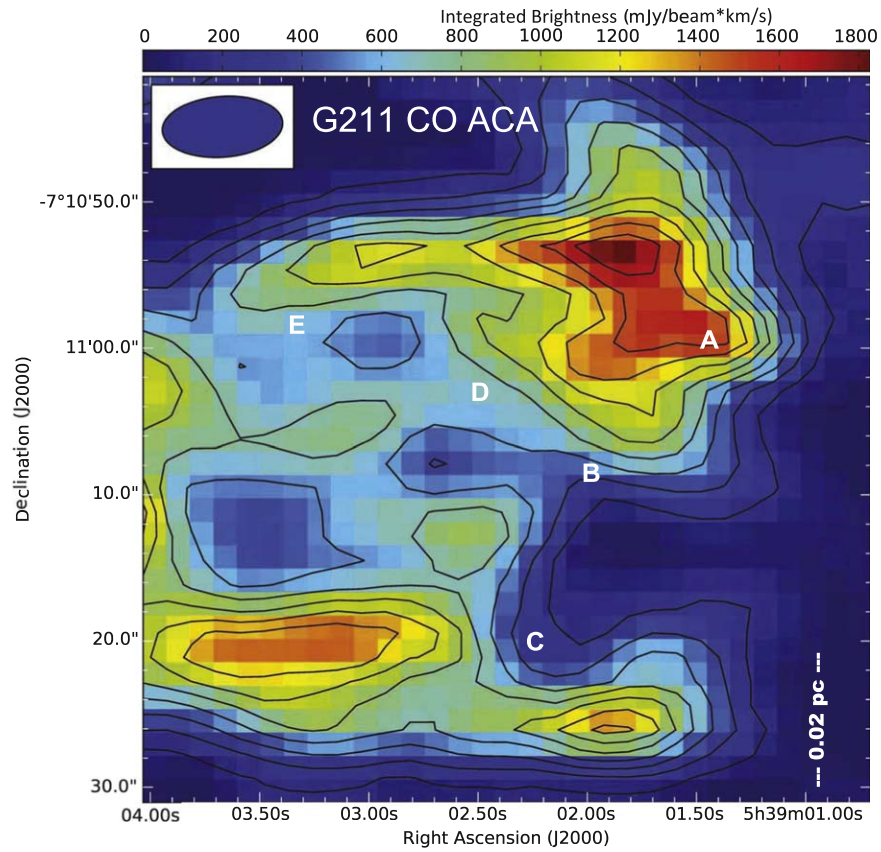


Figure 7. Information presented here is similar to that in Figure 4 with the velocity-integrated intensity maps of G211 in CO $J = 2-1$. 1 mJy beam^{-1} corresponds to 0.70 mK .

Table 4
Continuum Source Coordinate and Size from ACA

Core	IR association	R.A. (J2000) (h m s)	Decl. (J2000) ($^{\circ}$ ' ")	FWHM Major ($''$)	Source Size Minor ($''$)
G210	star-forming	5 37 56.60	-6 56 39.3	10.3	6.5
G211 A	starless	5 39 01.4	-7 11 00	8.0	4.5
G211 B	starless	5 39 01.79	-7 11 08	9.5	4.1
G211 C	starless	5 39 02.2	-7 11 19	11.4	9.8
G211 D	starless	5 39 02.4	-7 11 04	6.2	4.6
G211 E	starless	5 39 03.2	-7 10 59	7.9	3.6

Note. The FWHM source size is not deconvolved for the synthesized beam size. The continuum peak position error is estimated to be within $0.7''$ and $2''$, for G210 and for the other sources, respectively. The source size errors are about 3% and 10% for G210 and G211, respectively.

Table 5
Continuum Parameters from ACA

Core	Brightness (Jy beam $^{-1}$)	Flux Density (Jy)	R_{dust} (pc)	$N(\text{H}_2)_{\text{dust}}$ (cm $^{-2}$)	M_{dust} (\mathcal{M}_{\odot}^N)
G210	$2.8\text{E}-02$	$6.9\text{E}-02$	0.006	$2.8\text{E}+23$	0.72
G211 (all)	$8.0\text{E}-03$	$1.4\text{E}-02$	0.15
G211 A	$1.4\text{E}-03$	$1.9\text{E}-03$	0.0029	$3.3\text{E}+22$	0.019
G211 B	$8.2\text{E}-04$	$1.2\text{E}-03$	0.0034	$1.6\text{E}+22$	0.012
G211 C	$1.6\text{E}-03$	$6.6\text{E}-03$	0.009	$1.3\text{E}+22$	0.07
G211 D	$8.3\text{E}-04$	$8.8\text{E}-04$	0.009
G211 E	$3.3\text{E}-03$	$3.5\text{E}-03$	0.0012	$3.6\text{E}+23$	0.036

Note. The dust continuum radius R_{dust} is deconvolved for the synthesized beam size. G211D is not resolved with the synthesized beam. The flux error is about 20% in general, but is about 50% for G211E. The radius error is about 10%. The relative errors of the column density and mass are about 30%.

Table 6
ACA Line Parameters at the Intensity Peak Position

Core	N_2D^+	DNC	DCO^+	HCO^+
	T_R (K)	T_R (K)	T_R (K)	T_R (K)
G210	1.80	1.07	3.60	5.20
G211 A	0.95	1.90
G211 C	0.17	0.27	0.51	1.50
G211 D	0.22	0.22	0.42	...
G211 E	0.30	0.22	...	1.15

Note. The intensity error is about 10%.

Table 7
ACA Line Parameters Obtained After Averaging over Area (Figure 8)

Core	N_2D^+				DNC			DCO ⁺			HCO ⁺		
	T_R (K)	$\int T_A^* dv$ (K km s ⁻¹)	V_{LSR} (km s ⁻¹)	Δv (km s ⁻¹)	T_R (K)	V_{LSR} (km s ⁻¹)	Δv (km s ⁻¹)	T_R (K)	V_{LSR} (km s ⁻¹)	Δv (km s ⁻¹)	T_R (K)	V_{LSR} (km s ⁻¹)	Δv (km s ⁻¹)
G210	0.28	0.208	5.16	0.69	0.21	5.14	0.49	0.86	5.18	0.55	0.50	5.53	1.19
G211 A	0.74	3.48	0.22	1.03	3.59	0.30
G211 C	0.06	0.023	3.38	0.34	0.11	3.53	0.30	0.25	3.64	0.28	0.23	3.05	0.73
G211 D	0.09	0.030	3.12	0.32	0.11	3.23	0.28	0.31	3.19	0.29

Note. The errors of the intensity and line width are about 10%. The LSR velocity error is about 0.1 km s⁻¹.

antennas employed ranged from eight to ten. The baseline length ranged from 8.9 to 49 m.

The raw data were calibrated by the Joint ALMA Observatory and East-Asian ALMA Regional Center using the pipeline software of CASA (McMullin et al. 2007) version 4.7.2. Imaging was done by the authors manually using CASA 5.4.0. The continuum emission was collected from three 1.875 GHz wide continuum spectrum windows centered at 216.0, 244.0, and 267.0 GHz and also from emission-free channels of the line spectrum windows. We adopted 1.2 mm (242 GHz) as the representative wavelength (frequency) for the continuum emission. The synthesized beam size of the 1.2 mm continuum image was $7''.26 \times 3''.70$ with a position angle of $88^\circ.20$ for G210, and $7''.30 \times 3''.70$ with a position angle of $87^\circ.78$ for G211. The FWHM primary beam size was $42''$. The task “clean” of CASA was used for image deconvolution by using Briggs weighting with a “robust” parameter of 0.5.

The intensity is expressed in terms of the brightness temperature T_b . The rms noise level is 2.71 mJy beam⁻¹ for continuum, 170 mJy beam⁻¹ for CS, H¹³CN, H¹³CO⁺, and HN¹³C, and 130 mJy beam⁻¹ for the other molecular lines. Note that the primary beam response is not corrected for the maps but is corrected for the spectrum, flux density, line parameter, and physical parameters such as the column density.

3. Results

3.1. Results from Nobeyama Observations

Table 3 lists the line parameters obtained from observations with the Nobeyama 45 m telescope. For N_2D^+ and N_2H^+ , we show the results of hyperfine fitting. Both cores have bright emission from the deuterated molecules DNC ($J = 1-0$) and N_2D^+ ($J = 1-0$), which characterizes them as being close to the onset of star formation. From our earlier sample of 119 cores in Orion, the N_2D^+ ($J = 1-0$) detection rate was 49%, and the typical antenna temperature was T_A^* is 0.1–0.3 K. G210 and G211 are two bright cores in N_2D^+ emission with peak antenna temperatures of 0.45 K and 0.37 K for G210 and G211, respectively. For context, the brightest N_2D^+ core in Orion has T_A^* (N_2D^+) = 0.8 K. Figure 1 shows the N_2D^+ ($J = 1-0$) line spectra observed toward G210 and G211. The FWHM line widths Δv in N_2D^+ ($J = 1-0$) for G210 and G211 were derived to be 0.41 km s⁻¹ and 0.45 km s⁻¹, respectively, by fitting the hyperfine structure. These values are much narrower than the width of the deuterated molecular line toward massive protostellar objects (0.7–3 km s⁻¹; Fontani et al. 2006). Note that the line widths of HN¹³C and DNC are larger than those of the other lines, because we ignore their hyperfine structure

(Faure et al. 2007; van der Tak et al. 2009) when fitting. Observations of other cores are reported in Kim et al. (2020).

Figure 2 shows the N_2H^+ ($J = 1-0$) integrated intensity maps toward G210 and G211. Each map includes a chain of SCUBA-2 cores. Also, G210.82–19.47 North1 (G210), North2, and South are located along the ¹³CO filament #24 of Nagahama et al. (1998). G211.16–19.33 North1, North2, North 3 (G211), North4, and North5 are located along filament #26, while G211.16–19.33 North 3 (G211) and South are located along filament #28. Therefore, G211.16–19.33 North 3 (G211) is located around the intersection of filaments #26 and #28. Since the velocity difference between these two filaments is only 0.9 km s⁻¹, and given the fact that G211 is located at this the intersection, the filaments are likely physically connected. The N_2H^+ emission observed traces the backbone of these ¹³CO filaments.

The CS ($J = 2-1$) core FC-24 (Tatematsu et al. 1998), corresponding to a combination of G210.82–19.47 North1 (G210) and North2, has a line width of 2.06 km s⁻¹ (with a 50'' beam) and a half width at half maximum (HWHM) radius of 0.40 pc in CS ($J = 2-1$). The CS ($J = 1-0$) core TUKH101 (Tatematsu et al. 1993), corresponding to G211, has a line width of 0.99 km s⁻¹ (with a 36'' beam) and an HWHM radius of 0.15 pc in CS ($J = 1-0$). The line width in N_2D^+ toward G211 has been measured as 0.37 km s⁻¹ and is much narrower than the line width in CS by a factor of 2.7. It is likely that the nonthermal turbulent motions observed in the larger, less-dense CS core, have been largely dissipated in the high-density core center traced by N_2D^+ emission.

The column densities are calculated using the method described in Tatematsu et al. (2017). Excitation temperatures are derived for N_2D^+ and N_2H^+ through hyperfine component fitting, and that for the other molecules was assumed to be 8 K, which is half the typical dust temperature for PGCCs (16 K). The ratio of the excitation temperature to the gas kinetic temperature (assumed to be equal to the dust temperature) for the $J = 1-0$ molecular lines was assumed to be 50% from Figure 13 of Tatematsu et al. (2008). The deuterium fraction $N(\text{N}_2\text{D}^+)/N(\text{N}_2\text{H}^+)$ was derived as 0.32 ± 0.03 and 0.24 ± 0.05 for G210 and G211, respectively. For Orion cores, $N(\text{N}_2\text{D}^+)/N(\text{N}_2\text{H}^+)$ ranges from 0.04 to 0.4 with a median of 0.2 for star-forming cores and from 0.06 to 0.4 with a median of 0.2 for starless cores. $N(\text{DNC})/N(\text{HN}^{13}\text{C})$ is 4.0 ± 2.8 and 3.9 ± 0.8 for G210 and G211, respectively, which correspond to $\text{D}/\text{H} = 0.067 \pm 0.047$ and 0.065 ± 0.01 by assuming ¹²C/¹³C = 60 (Savage et al. 2002). For Orion cores, $N(\text{DNC})/N(\text{HN}^{13}\text{C})$ ranges from 1.0 to 13.7 with a median of 2.7 for star-forming cores and from 0.7 to 7.7 with a median

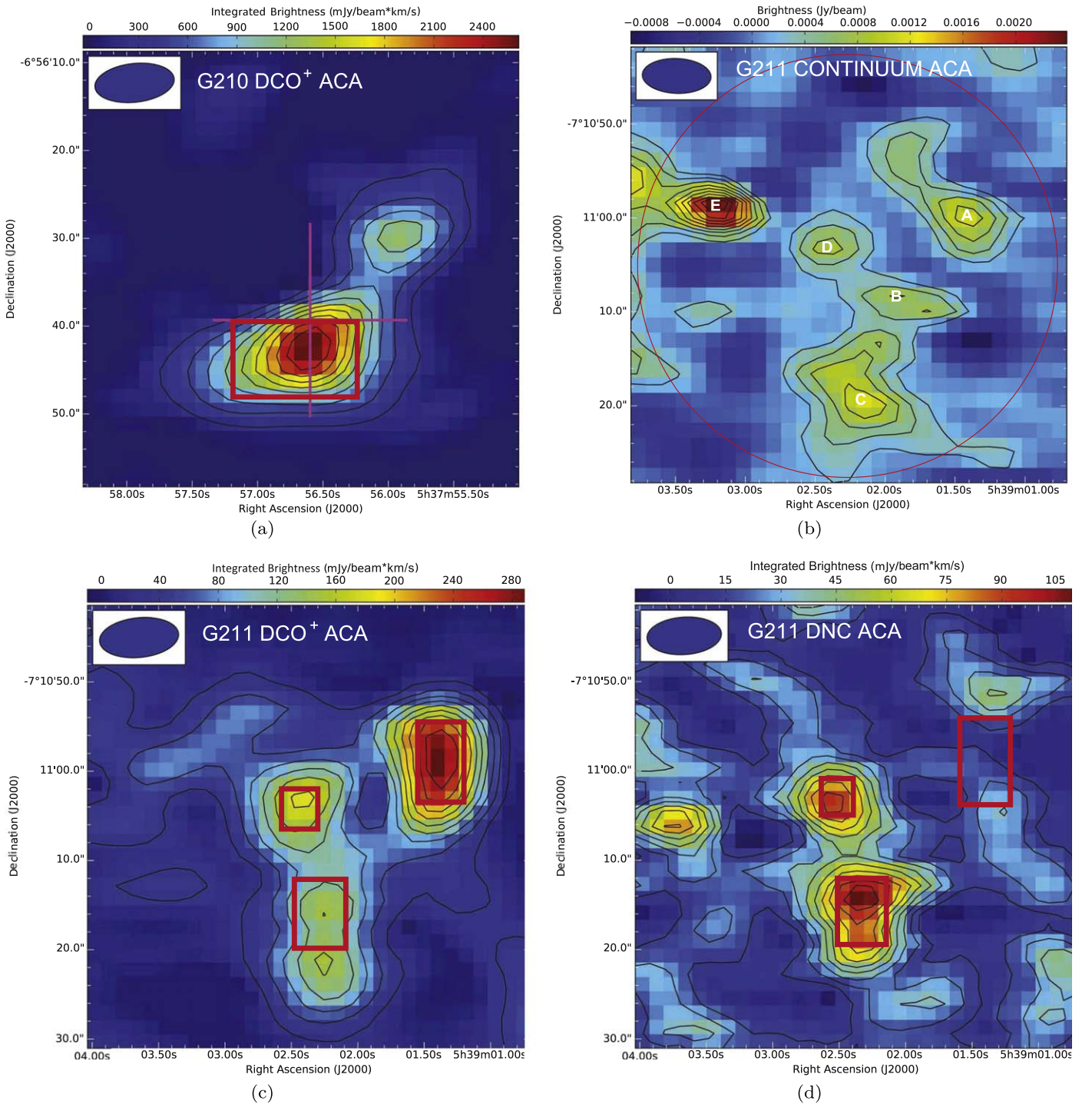


Figure 8. The red rectangles depict the averaging areas used for the intensity and the spectrum. Panel (a): DCO⁺ map toward G210; panel (b): continuum map toward G211; panel (c): DCO⁺ map toward G211; and panel (d): DNC map toward G211.

of 3.8 for starless cores (Kim et al. 2020). G210 and G211 are relatively high deuterium fraction cores in Orion.

3.2. Results from the ACA Observations

Figure 3 shows that in the 1.2 mm continuum, G210 exhibits only a single peak while G211 exhibits five emission peaks in the fields of view. The G210 dust continuum core is associated with the Herschel protostar HOPS 157. The primary-beam-corrected 1.2 mm continuum flux density is 69 mJy, measured by fitting a two-dimensional Gaussian to the map using the task

“imfit” in CASA. The SCUBA-2 flux density at 850 μm is 713 mJy with a beam size of 14". If we assume a spectral index of $\beta = 1.8$ (Lombardi et al. 2014), 41% of the dust emission is recovered by the ACA observations. For G211, the sum of the primary-beam-corrected 1.2 mm continuum flux densities of peaks G211A–E is 14 mJy. The SCUBA-2 flux density at 850 μm is 281 mJy with a beam size of 14". Again, if we assume a spectral index of $\beta = 1.8$ (Lombardi et al. 2014), 21% of the dust emission is recovered by the ACA observations.

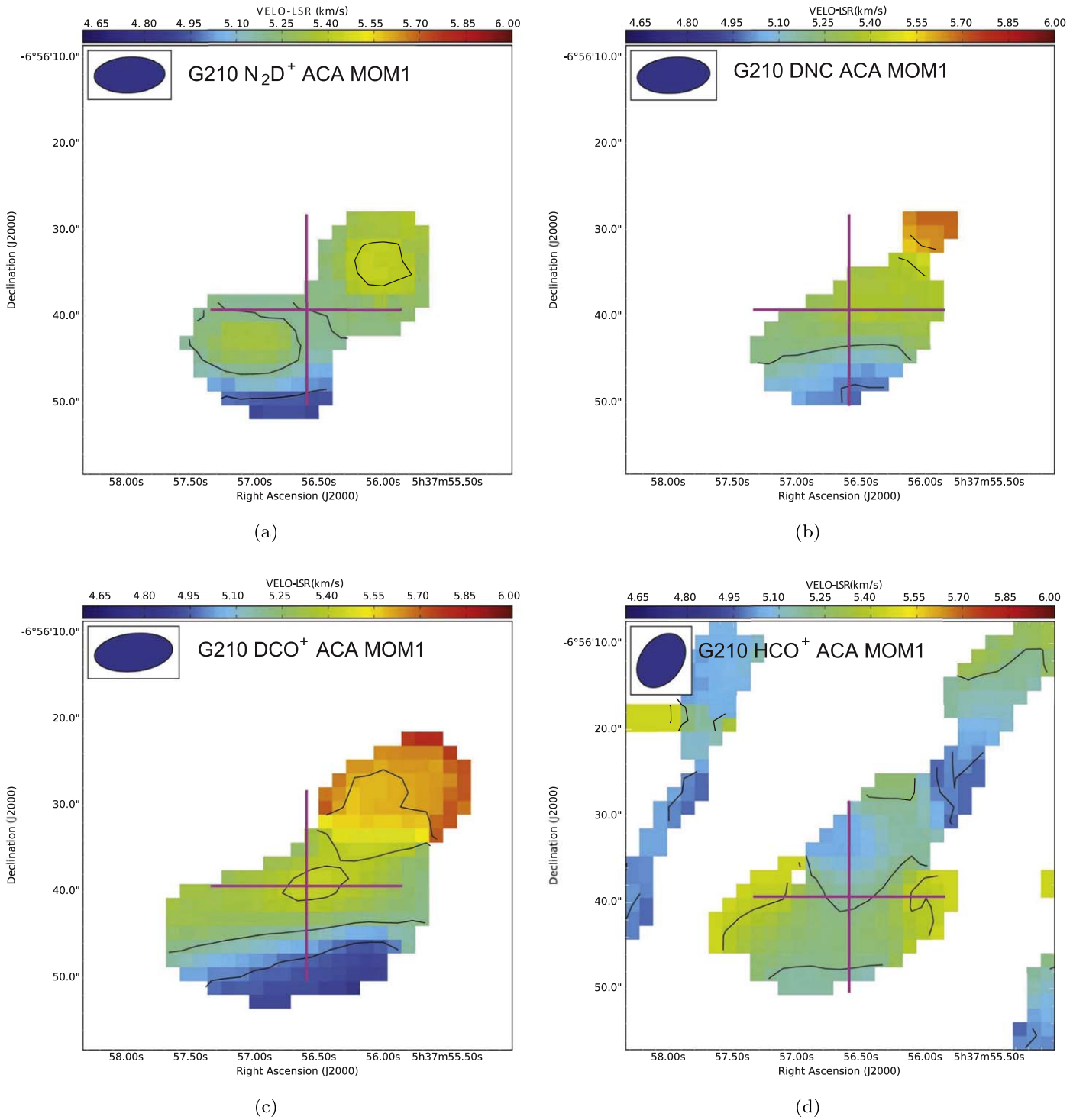


Figure 9. The intensity-weighted radial velocity maps of G210 are as follows: panel (a) N_2D^+ $J = 3-2$; panel (b): DNC $J = 3-2$; panel (c): DCO^+ $J = 3-2$; and panel (d): HCO^+ $J = 3-2$. The contour interval is 0.2 km s^{-1} .

In addition to the 1.2 mm continuum, G210 was detected in N_2D^+ ($J = 3-2$), DNC ($J = 3-2$), DCN ($J = 3-2$), DCO^+ ($J = 3-2$), HCO^+ ($J = 3-2$), CS ($J = 5-4$), HCN ($J = 3-2$), HCO^+ ($J = 3-2$), H^{13}CO^+ ($J = 3-2$), H^{13}CN ($J = 3-2$), and CO ($J = 2-1$) with the ACA 7 m Array. Integrated intensity maps are shown in Figures 4 and 5 (the CO distribution will be shown later). Note that the N_2D^+ map shows two symmetric peaks centered on the dust continuum peak (plus). The two

peaks have similar intensities, with the weaker peak being 60%–70% as bright as the stronger one. The CS ($J = 5-4$), H^{13}CO^+ ($J = 3-2$), and H^{13}CN ($J = 3-2$) integrated intensities, however, are concentrated toward the dust continuum peak. The DCO^+ ($J = 3-2$) and DNC ($J = 3-2$) integrated intensities show a hint of the double peaks, but the brightnesses of the two peaks are rather different. Furthermore, the peak positions in these latter lines are different from those of the

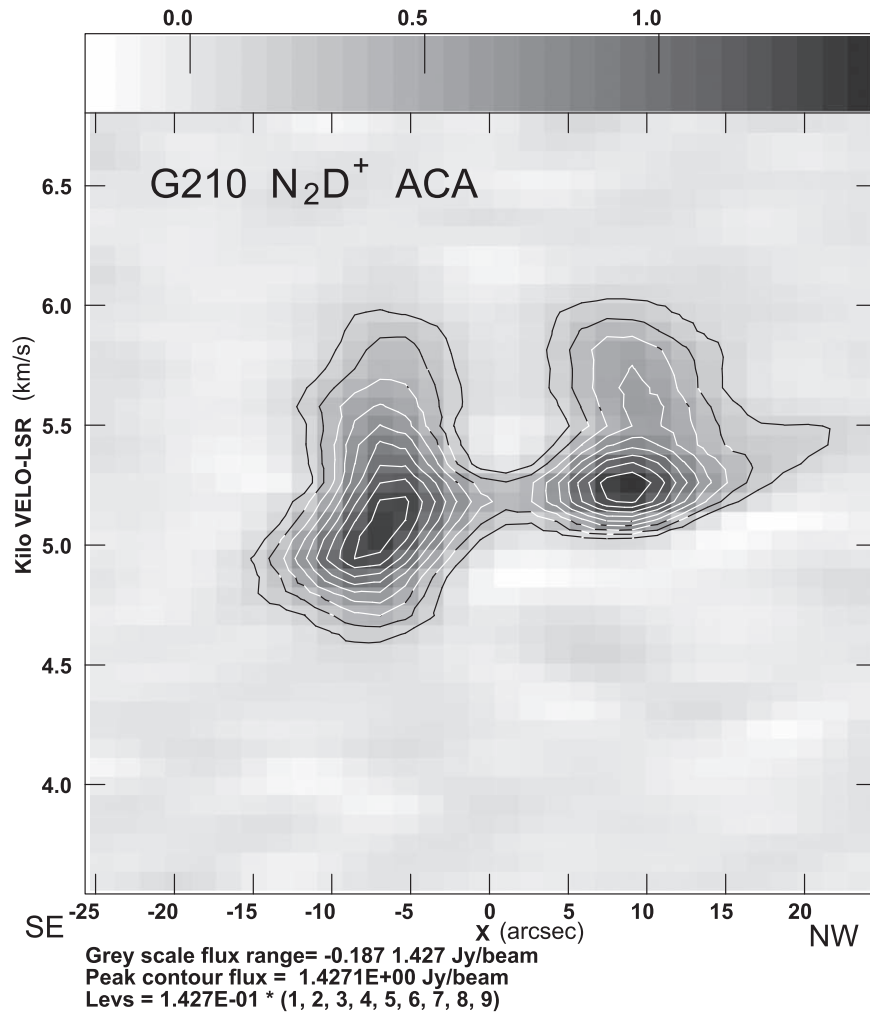


Figure 10. The position–velocity diagram in N_2D^+ emission along the strip line passing through two N_2D^+ peaks of G210 with a P.A. angle of 51° . The emission is averaged across the $5''$ width perpendicular to the strip line. The position offset X is defined with respect to the position of the protostar HOPS 157.

N_2D^+ peaks. Molecules that are not deuterated do not show the double peaks and likely represent the underlying column density and temperature distribution, which increase toward the position of the protostar, in a simple manner.

G211 was detected in DCO^+ ($J = 3-2$), HCO^+ ($J = 3-2$), DNC ($J = 3-2$), N_2D^+ ($J = 3-2$), and CO ($J = 2-1$) but was not detected in the other lines.

Figures 6 and 7 show the integrated intensity maps of G211 in various molecular lines. The distribution of these molecular lines is very different from the dust continuum distribution. DCO^+ and HCO^+ have intensity maxima toward G211A. N_2D^+ and DNC have intensity maxima near G211C, but are displaced toward G211B. G211E is not bright but is weakly detected in HCO^+ , N_2D^+ , and DNC . We see appreciable differences in molecular line distribution, which most likely represents distinct chemical variation. The distribution of DCO^+ and HCO^+ are similar, and those of N_2D^+ and DNC are also similar. The CO distribution (Figure 7) has local peaks corresponding to G211A and C.

3.3. Observed Parameters from the ACA

In Tables 4 and 5, we summarize the result of the continuum observations. Note that the FWHM major and minor axes in Table 4 are not corrected for the synthesized beam size, while the radius R , brightness, and flux density are corrected for

the synthesized beam size. The synthesized beam size is $7''.3 \times 3''.7$. The cataloged position of HOPS 157 (R.A. = $5^{\text{h}}37^{\text{m}}56^{\text{s}}.57$; decl. = $-6^\circ56'39''.1$) is almost identical to the G210 continuum source position within $1''$. We calculate the mass M_{dust} from the flux density of the dust continuum emission. The gas-to-dust mass ratio is assumed to be 100, and the opacity of dust grains with thin ice mantles at a gas density of 10^6 cm^{-3} from Ossenkopf & Henning (1994) is adopted. The derived dust continuum mass of G210 ($0.80 \mathcal{M}_{\odot}^{\text{N}}$) is twice the Herschel best-fit envelope mass of the central compact component within 2500 au or $6''$ ($0.38 \mathcal{M}_{\odot}^{\text{N}}$; Furlan et al. 2016). The difference in the flux density ($6.9 \times 10^{-2} \text{ Jy}$) and peak brightness ($2.8 \times 10^{-2} \text{ Jy beam}^{-1}$) with a $\sim 5''$ beam is also approximately two, which is consistent with the above difference. The factor-of-two difference means that there are two components: half of the mass is located in the point-like source, while the other half is located in the outer part. The masses of the sub-cores in G211 are less than $0.1 \mathcal{M}_{\odot}^{\text{N}}$, and it seems natural that G211 is starless. These sub-cores need to accrete more mass from outside to form protostars. This topic will be discussed in Section 4.3.

Next, we summarize the line observations with the ACA. Line intensities at the integrated intensity peak positions and averaged over the areas are listed in Tables 6 and 7, respectively. Figure 8 depicts the regions where the emission

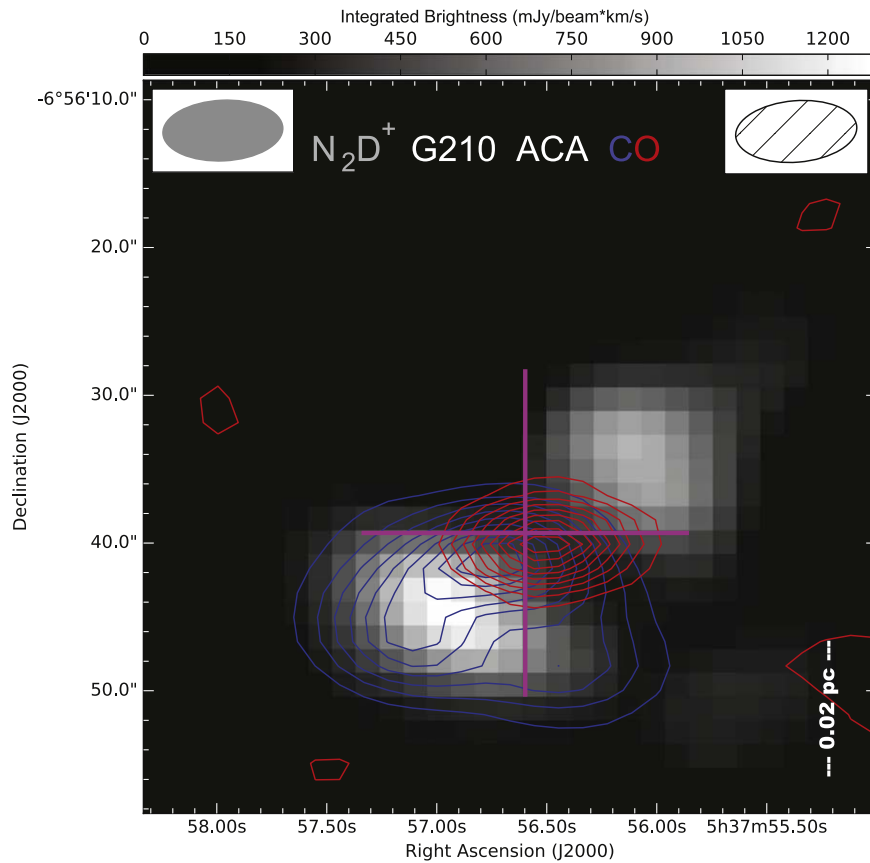


Figure 11. ACA 7 m outflow map of CO ($J = 2-1$) toward the star-forming core G210 superimposed on the grayscale N_2D^+ map. The integration ranges are -15.0 to 3.3 km s^{-1} and 10.5 to 13.0 km s^{-1} for the blue and red lobes, respectively. The contour interval is 10% of the maximum intensity of each lobe, where the maximum values are $2.7 \text{ Jy beam}^{-1} \text{ km s}^{-1}$ and $4.9 \text{ Jy beam}^{-1} \text{ km s}^{-1}$ for blue and red lobes, respectively. The pink plus symbol shows the location of the continuum peak. The ovals at the top-left and top-right corners illustrate the synthesis beam sizes for the N_2D^+ and CO data, respectively.

is averaged for spectra. The map is not primary-beam corrected; however, the brightness (and the spectra shown later) are primary-beam corrected to derive physical parameters.

4. Discussion

G210 shows a simple structure, whereas G211 shows complicated structures. In this section, we discuss the properties of each object.

4.1. G210

We first discuss the distribution of deuterated molecules in G210 (Figure 4). Deuterated molecules are less abundant in warmer gas because the parent molecule for deuterated molecules, H_2D^+ , is easily destroyed by CO evaporated from the dust in warmer gas (Fontani et al. 2006). Indeed, gas in the vicinity of a protostar should be warm, and as a result, it is reasonable to expect that the distribution of deuterated molecules will be depressed toward the protostar. Nevertheless, Figure 4 shows that DCN, unlike other deuterated molecules, traces warm molecular gas near the protostar. Similarly, Gerner et al. (2015) showed that DCN traces warmer regions better than DNC does. This difference could be the reason for the single-peak DCN distribution. Non-deuterated molecules do not show the spatial double peaks either (Figure 5). If optically thin, they likely represent the underlying column density and

temperature distributions, which should increase toward the position of the protostar, in a simple manner.

Figure 9 shows the moment-1, intensity-weighted radial velocity maps of G210. There is a barely significant velocity difference between the two N_2D^+ peaks (Figure 9(a)). $DCO^+ J = 3-2$ and $DNC J = 3-2$, however, show a velocity gradient from the southeast (blueshifted) to the northwest (redshifted; Figures 9(b) and (c)). Because N_2D^+ is more optically thin, it likely traces better the inner part of the core than DCO^+ and DNC do. Our finding is similar to that by Puanova et al. (2018): N_2D^+ and N_2H^+ show smaller velocity gradients than the lower-density tracers DCO^+ and $H^{13}CO^+$ in cores in the Taurus dark cloud L1495. One possible interpretation for the two N_2D^+ peaks without a significant velocity difference is that we detect an edge-on disk in N_2D^+ with a radius of $8-10''$ or 4000 au . With our spatial resolution, however, it is impossible to see the protoplanetary disk ($\sim 100 \text{ au}$). The DCO^+ distribution is larger than the N_2D^+ distribution. DCO^+ and DNC likely trace the outer part of the core, which, as seen here, is expected to be more turbulent and irregular in distribution and kinematics. On the other hand, the N_2D^+ distribution may trace a nonrotating edge-on pseudo-disk. Figure 10 shows the position-velocity diagram along the strip line passing through the two N_2D^+ peaks with a P.A. angle of 51° . Looking at the intensity maxima, the velocity difference of the two N_2D^+ peaks is only about 0.17 km s^{-1} , which is close to the spectral resolution (0.16 km s^{-1}). Therefore, the velocity difference is marginal, and we cannot ascertain clearly whether there is a velocity

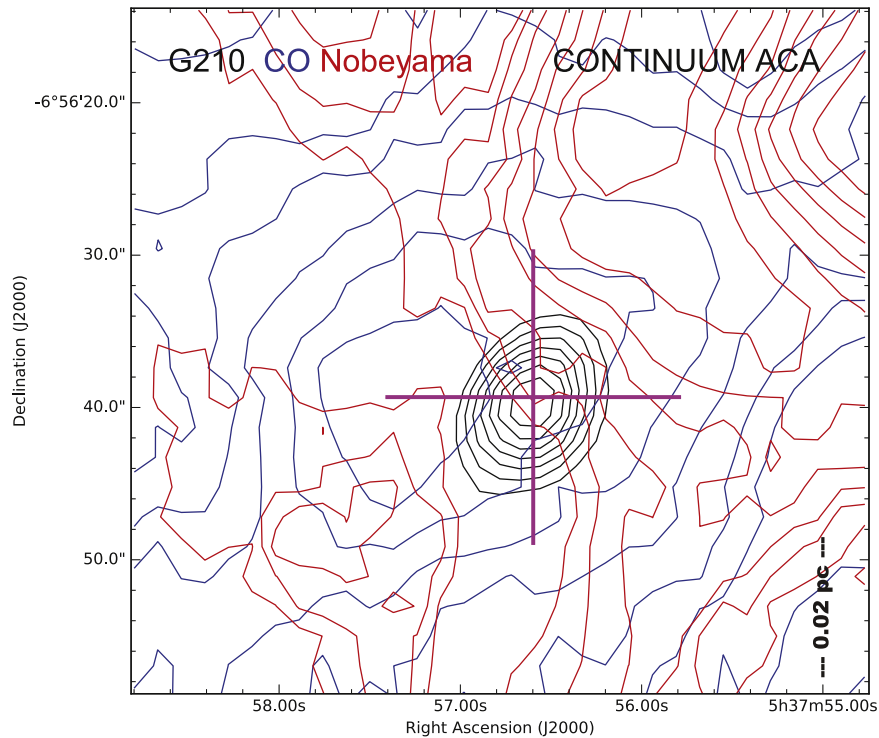


Figure 12. Outflow map of CO ($J = 1-0$) toward the star-forming core G210 from the data of the Nobeyama 45 m telescope legacy program “Star Formation” (Nakamura et al. 2019) through the Japanese Virtual Observatory superposed on the continuum map. The integration ranges are the same as those in Figure 11. The contour levels are 30, 40, 50, 60, 70, 80, and 90% of the maximum intensity of each lobe, where the maximum values are 2.9 K km s^{-1} and 1.1 K km s^{-1} for the blue and red lobes, respectively. The plus shows the location of the continuum peak. The effective spatial resolution is $21''.7$.

gradient or not. The radius of 4000 au is between a large value of $\sim 15,000\text{--}30,000$ au of the archetypal pseudo-disk associated with the Class 0 protostar L1157 (Looney et al. 2007) and a small value of 165–192 au around a proto-brown dwarf (Riaz et al. 2019). Ohashi et al. (1997) investigated the specific angular momentum of the rotating protoplanetary disk and the (collapsing) envelope (or pseudo-disk) as well as the molecular cloud core. The radius of 4000 au corresponds to a boundary between the two regimes of disks (the specific angular momentum is almost constant) and cores (the specific angular momentum decreasing with decreasing radius). It is possible that G210 has a rotating protoplanetary disk with a size of ~ 100 au, similar to the disk associated with the low-mass protostar IRAS 04368+2557 in L1527 (Sakai et al. 2014). Higher-resolution studies are desired to investigate this possibility.

Given that the N_2D^+ distribution appears to trace a nonrotating (or slowly rotating) edge-on pseudo-disk, we wonder how the associated molecular outflow looks. Figure 11 shows the distribution of the high-velocity CO gas. An edge-on disk is expected to have a symmetric molecular outflow oriented perpendicular to the disk plane; however, the distribution of the CO lobes is not consistent in this view. Instead, the red lobe is very compact ($<5''$ or <0.02 pc), while the blue lobe maximum displacement is larger ($10''$ or 0.03 pc). If we take 18 km s^{-1} and 9 km s^{-1} (the maximum velocity offset from the systemic velocity) for the expansion speed of the blue and red lobe, respectively, the dynamical timescale is as short as 2×10^3 yr. This short duration seems consistent with the interpretation that G210 is immediately after the onset of star formation. The dynamical timescale here, however, is

calculated from the maximum lobe extension and the maximum velocity offset. This latter value may be quite underestimated for an edge-on system, while the former may also be underestimated due to missing flux from broader emission. Indeed, we wonder if the missing flux of CO may affect the appearance of the outflow. Figure 12 shows the map of outflow from CO ($J = 1-0$) data of the “Star Formation” legacy program with the Nobeyama 45 m telescope (Nakamura et al. 2019). Here, the blue lobe is consistently seen, but the red lobe is not. The widespread red CO emission on the northwestern side is associated with the quiescent ambient molecular cloud rather than molecular outflows. Due to this extended CO emission, it is hard to isolate the distribution of the red lobe on this map. For further comparison, Figure 13 shows the HCO^+ outflow map from our ACA observation. Relative to CO, it is harder to recognize the outflow configuration, but an outflow axis is discernable in the east–west direction. At any rate, there is no clear evidence that the direction of the outflow lobes is perpendicular to the line connecting the two N_2D^+ peaks as could be expected if the N_2D^+ distribution represents a nonrotating (or slowly rotating) edge-on pseudo-disk. It is thus difficult to explain the N_2D^+ distribution and the outflow distribution consistently.

Although Poidevin et al. (2010) and Tatematsu et al. (2016) suggest that there is no strong correlation among the directions of local magnetic fields, core elongation, core rotation, and molecular outflows, we check the orientations of the filament and magnetic field. The direction of the line connecting the two N_2D^+ peaks (Figure 4(a), position angle (P.A.) = 51°) is almost parallel to that of the larger N_2H^+ filament containing

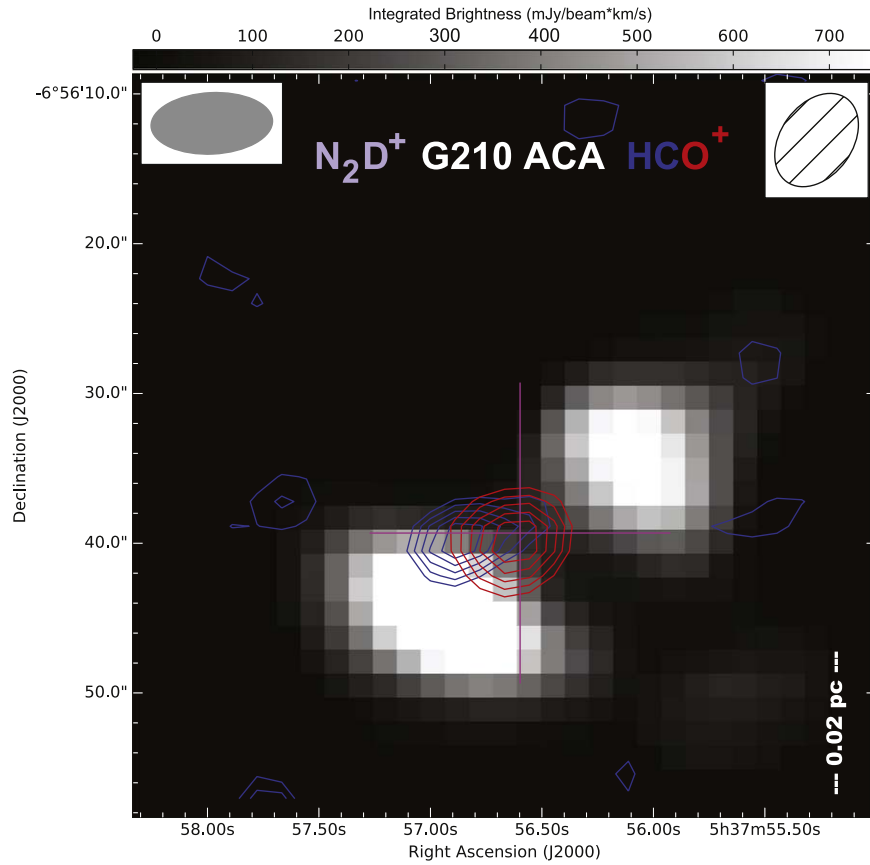


Figure 13. ACA 7 m outflow map of HCO^+ ($J = 3-2$) toward the star-forming core G210 superimposed on the grayscale N_2D^+ map. The blue and red contours represent the blue and lobes, respectively. The integration ranges are $2.3-4.3 \text{ km s}^{-1}$ and $6.0-8.0 \text{ km s}^{-1}$ for the blue and red lobes, respectively. The contour levels are 50, 60, 70, 80, and 90% of the maximum intensity of each lobe, where the maximum values are $0.75 \text{ Jy beam}^{-1} \text{ km s}^{-1}$ and $0.43 \text{ Jy beam}^{-1} \text{ km s}^{-1}$ for the blue and red lobes, respectively. The plus sign shows the location of the continuum peak. The oval at the top illustrates the synthesis beam size.

Table 8
Column Density and Abundance from ACA

Core	$N(\text{N}_2\text{D}^+)$ (cm^{-2})	$N(\text{DNC})$ (cm^{-2})	$N(\text{DCO}^+)$ (cm^{-2})	$X(\text{N}_2\text{D}^+)$	$X(\text{DNC})$	$X(\text{DCO}^+)$
G210	$1.8\text{E}+12$	$3.5\text{E}+11$	$1.0\text{E}+12$	$6.4\text{E}-12$	$1.3\text{E}-12$	$3.7\text{E}-12$
G211 A	$3.4\text{E}+11$	$1.0\text{E}-11$
G211 C	$2.0\text{E}+11$	$1.1\text{E}+11$	$1.4\text{E}+11$	$1.6\text{E}-11$	$9.0\text{E}-12$	$1.1\text{E}-11$
G211 D	$2.6\text{E}+11$	$1.1\text{E}+11$	$1.9\text{E}+11$

Note. The relative errors of the column density and abundance are about 30%.

G210 (Figure 2(a), P.A. = 44°). The direction of the global magnetic field for this region is P.A. = 60° from the measurement with the Planck satellite (Soler et al. 2018), almost parallel to the line connecting the two N_2D^+ peaks and the N_2H^+ filament.

4.2. G211

In G211 (Figure 6), we see large differences in the spatial distribution of molecular emission, which could represent differences in abundances (and optical depths). To explore this idea, we first compare column densities calculated through the standard local thermodynamic equilibrium (LTE) method assuming that the line is optically thin. We assume the gas kinetic temperature to be 16 K from the dust temperature of the associated Planck cold clump. The H_2 volume density estimated from the dust continuum emission is of the order

10^{6-7} cm^{-3} , while the critical densities $n_{\text{cr}}(\text{H}_2)$ of the observed $J = 3-2$ lines are of the order 10^{7-8} cm^{-3} . To obtain estimates of the excitation temperature, we ran the RADEX software³¹ (van der Tak et al. 2007). From test values of $N(\text{H}_2) = 3 \times 10^6 \text{ cm}^{-3}$, $T_{\text{kin}} = 20 \text{ K}$, $\Delta v(\text{DCO}^+) = 0.5 \text{ km s}^{-1}$, $N(\text{DCO}^+) = (1-10) \times 10^{12} \text{ cm}^{-2}$, and $T_R(\text{DCO}^+ J = 3-2) = 0.3-1 \text{ K}$, we obtain $T_{\text{ex}} = 15 \text{ K}$ (almost fully thermalized) and assume this value for all molecular lines observed with the ACA. Table 8 summarizes the resulting column densities and abundances. For a comparison, we also include G210. We see large variation in the column density ratios among sub-cores in G211 and between G210 and G211. The HCO^+ profiles show hints of (self) absorption (double peaks, Figures 14 and 16), and the line optical depth should be very large. Therefore, we exclude

³¹ <http://var.sron.nl/radex/radex.php>

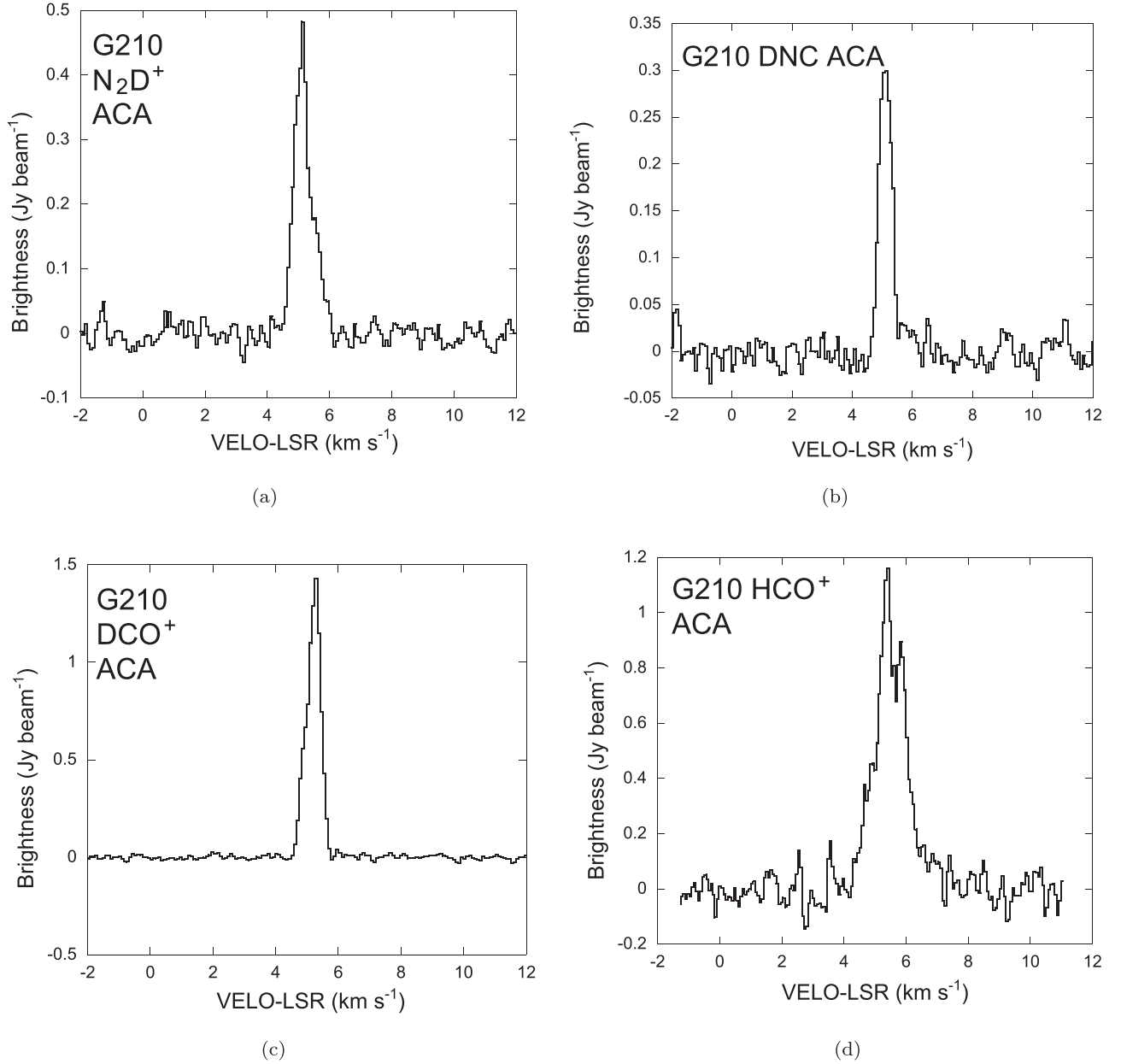


Figure 14. Line profiles of G210: panel (a): $\text{N}_2\text{D}^+ J = 3-2$; panel (b): $\text{DNC } J = 3-2$; panel (c): $\text{DCO}^+ J = 3-2$; and panel (d): $\text{HCO}^+ J = 3-2$.

Table 9
Mass and Virial Mass from ACA

core	M_{dust} ($\mathcal{M}_{\odot}^{\text{N}}$)	$\Delta v(\text{DCO}^+)$ (km s^{-1})	M_{vir} ($\mathcal{M}_{\odot}^{\text{N}}$)	α_{vir}
G210	0.72	0.55	0.39	0.5
G211 (all)	0.15
G211 A	0.019	0.22	0.030	1.5
G211 C	0.07	0.28	0.15	2.1
G211 D	0.009	0.29

Note. The errors of the mass and virial parameter are about 30%. The line-width error is about 10%.

this molecule from the column density estimation. Regarding the relative evolutionary stage of the sub-cores, the non-detection of N_2D^+ emission in G211A suggests this sub-core is young, while relatively bright N_2D^+ emission in G211C

suggests it is a more evolved starless core. We judge that, among G211A, C, and D, G211A is the youngest, and G211C is the most evolved starless core, from the relative intensity of the N_2D^+ emission compared with the DCO^+ and HCO^+ emission. Note also that G211E is not prominent in molecular lines. It is likely that G211E shows the local maximum of the core column density, but its density is not high enough to excite the $J = 3$ level of the observed molecules.

G211A, C, and D have different velocities (3.48 km s^{-1} , 3.64 km s^{-1} , and 3.19 km s^{-1} , respectively, in DCO^+). Sub-cores G211A, C, and D have FWHM line widths of $0.22-0.29 \text{ km s}^{-1}$ (Table 7). Because the FWHM thermal line width of DCO^+ for 20 K is 0.17 km s^{-1} , sub-cores do not appear purely thermal. G211 is very clumpy, and its substructures have different chemical compositions and radial velocities, suggesting that the G211 core is not dynamically and chemically settled, and consists of velocity-coherent sub-cores.

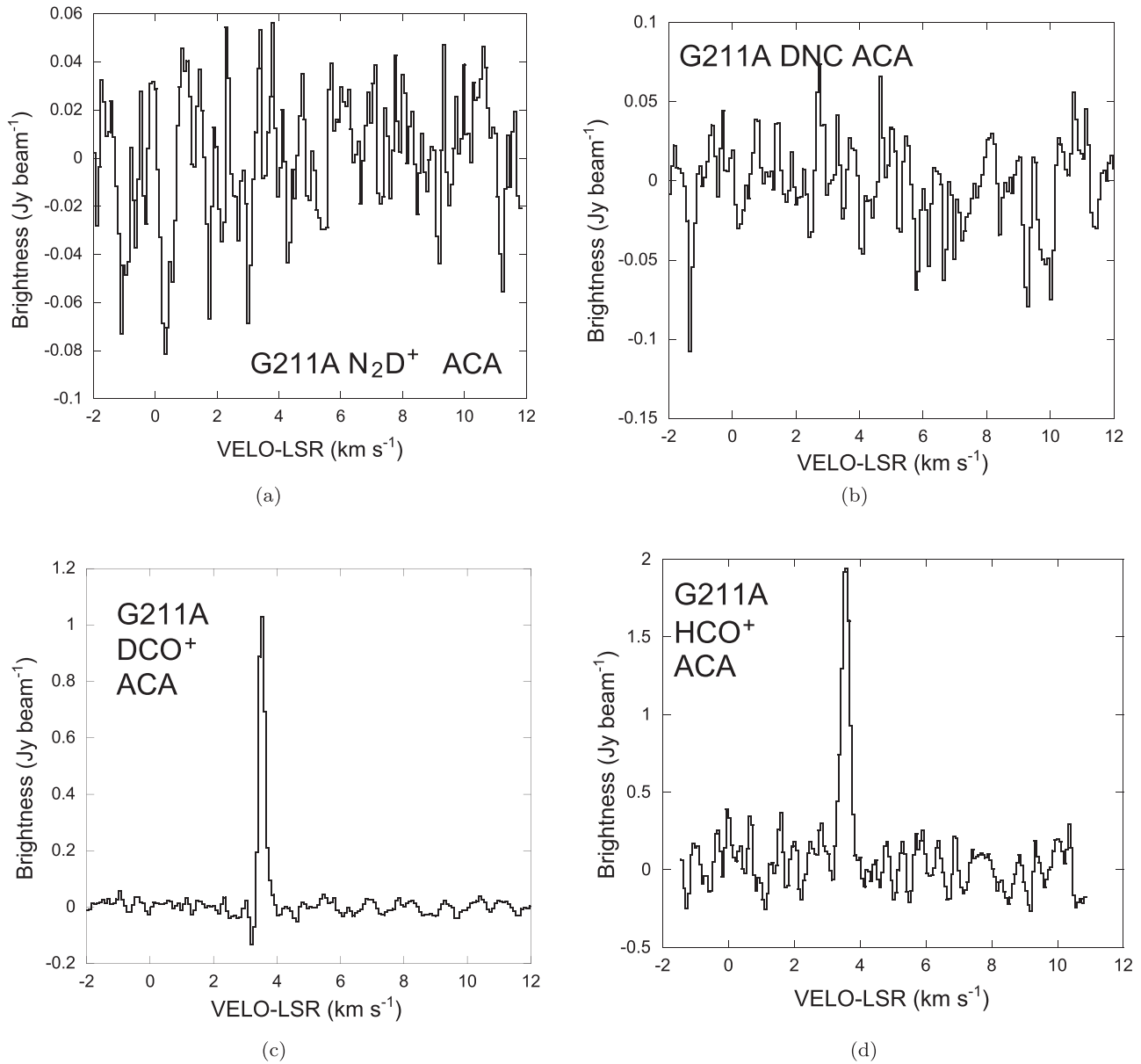


Figure 15. Line profiles of G211A: panel (a): $\text{N}_2\text{D}^+ J = 3-2$; panel (b): $\text{DNC } J = 3-2$; panel (c): $\text{DCO}^+ J = 3-2$; and panel (d): $\text{HCO}^+ J = 3-2$.

4.3. Fragmentation, Virial Mass, and Motion

Ohashi et al. (2018) found a hint of thermal Jeans fragmentation toward the starless core TUKH122 in the same cloud as G210 and G211, Orion A. For example, the separation of its condensations is ~ 0.035 pc, consistent with the thermal Jeans length at a density of $4.4 \times 10^5 \text{ cm}^{-3}$ and a temperature of 12 K. For comparison, the dust continuum map of G211 (Figure 3(b)) shows separations among sub-cores of about $10''$ or 0.02 pc, similar to the value of Ohashi et al. (2018). Hence, our data support the idea of thermal Jeans fragmentation in the pre-stellar phase. In the Taurus molecular cloud, which is the archetypal nearby dark cloud, we observe examples of fragmentation of filaments. For example, the Miz2, Miz7, Miz8b, and Miz8 cores (Tatematsu et al. 2004) are spaced at equal intervals of $\sim 1/3$ or 0.07 pc along their host filament. If we assume different densities of 1×10^5 (Onishi et al. 2002), 3×10^5 (Tatematsu et al. 2014), and $1 \times 10^6 \text{ cm}^{-3}$ and a common temperature of 10 K for Taurus cloud cores,

TUKH122-n in Orion, and G211 (judging from those for G211A and G211C), respectively, the spatial spacing can be interpreted in terms of thermal Jeans fragmentation. Sanhueza et al. (2019) also reported thermal Jeans fragmentation in IRDC clumps. Moreover, we note that the observed FWHM line width of N_2D^+ is $0.32\text{--}0.34 \text{ km s}^{-1}$ for G211, and the corresponding effective sound speed (line-of-sight velocity dispersion $\sigma = \text{FWHM linewidth} / \sqrt{8 \ln 2}$) corresponding to 2.33 u (the mean molecular weight per particle in terms of the atomic mass unit; Fuller & Myers 1992; Aso et al. 2000) is 0.23 km s^{-1} , which is very close to the sound speed for 10 K (0.19 km s^{-1}). It seems that turbulence has been almost completely dissipated in these sub-cores.

Next, we discuss the virial masses of G210 and G211 (Table 9). The virial mass M_{vir} is calculated from the radius R ($\text{HWHM} = \text{FWHM}/2$) deconvolved for the synthesized beam size of the dust continuum map (Table 5) and the FWHM line width in DCO^+ , assuming a constant density sphere (MacLaren et al. 1988). We adopt DCO^+ , because its line emission is

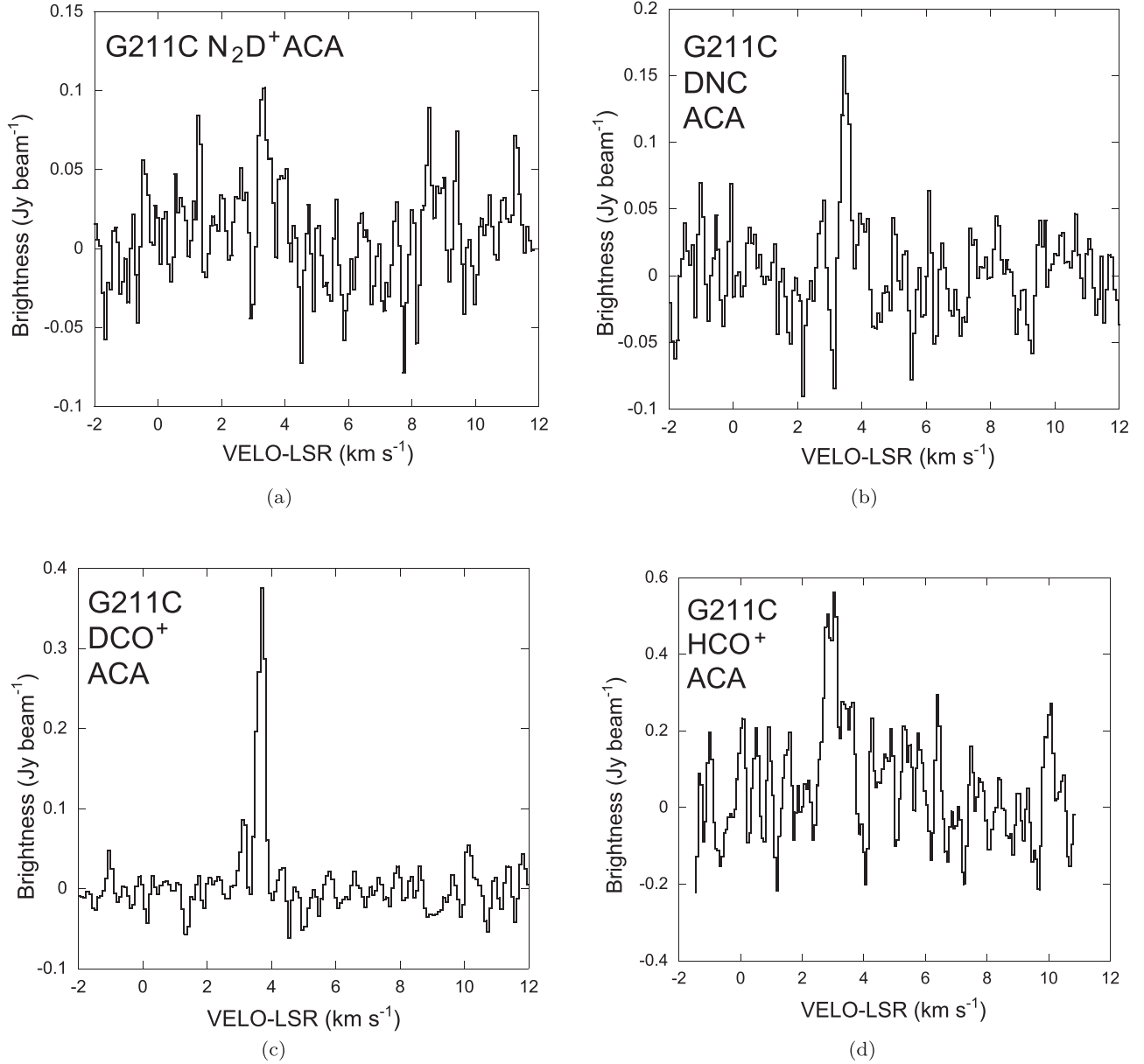


Figure 16. Line profiles of G211C: panel (a): N₂D⁺ $J = 3-2$; panel (b): DNC $J = 3-2$; panel (c): DCO⁺ $J = 3-2$; and panel (d): HCO⁺ $J = 3-2$.

detected from both cores and delineates the core relatively well. The virial parameter α_{vir} is defined as $\alpha_{\text{vir}} = M_{\text{vir}}/M_{\text{dust}}$.

G211 is divided into several sub-cores (0.01–0.07 $\mathcal{M}_{\odot}^{\text{N}}$) having virial parameters of 1.5–2.1. In high-mass star-forming regions, small virial parameters have been reported (Kauffmann et al. 2013); however, this is not the case for G211. The evolved starless core G211C has a larger virial parameter ($\alpha_{\text{vir}} = 2.1$) than the younger starless core G211A ($\alpha_{\text{vir}} = 1.5$). G210 is a solar-mass object, and its virial parameter is 0.5. However, the sample number is too small for a statistical study of the virial parameter of the sub-core, and further studies are desired. In the larger scale, the CS ($J = 1-0$) core TUKH101 (Tatematsu et al. 1993) corresponding to G211 has an LTE mass M_{LTE} of 27 $\mathcal{M}_{\odot}^{\text{N}}$ and a virial mass M_{vir} of 30 $\mathcal{M}_{\odot}^{\text{N}}$, and the virial parameter $\alpha_{\text{vir}} = M_{\text{vir}}/M_{\text{LTE}}$ is close to unity. Kong et al. (2017) studied high-mass starless cores in IRDCs with the ALMA in the continuum and lines including N₂D⁺, and they concluded that the six “best” N₂D⁺

cores are consistent with virial equilibrium of pressure confined cores. The virial parameter ranges from 0.2 to 0.75. We wonder if there are environmental differences among nearby dark clouds, general GMCs (regions outside IRDCs), and IRDCs, because the external pressure is likely to differ (Tatematsu et al. 1993; Aso et al. 2000; Heyer et al. 2009).

Finally, we explore whether there are any hints of collapse or expansion motions associated with G210 and G211 cores. Figures 14–17 represent the line profiles averaged over the specific area for G210 and G211 depicted in Figure 8. Occasionally, we see absorption due to missing flux for extended emission. For HCO⁺, the absorption is severe. We see the wing emission in HCO⁺ toward G210. For the continuum emission, 41% and 21% of the SCUBA-2 flux densities were recovered with the ACA 7 m Array for G210 and G211, respectively. Deuterated molecules trace high-density ($\gtrsim 10^5 \text{ cm}^{-3}$) gas, and their intensity distribution is

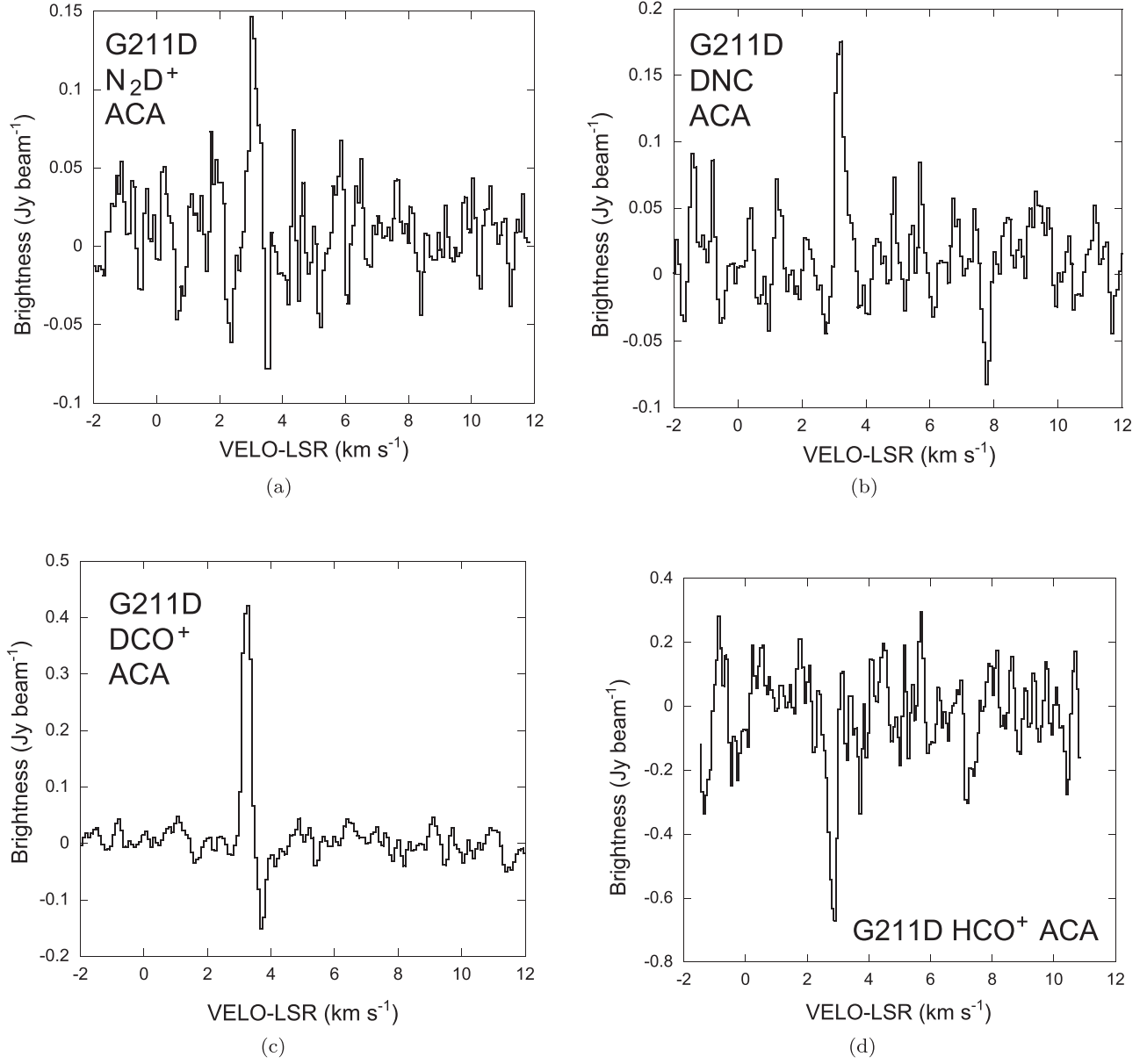


Figure 17. Line profiles of G211D: panel (a): $\text{N}_2\text{D}^+ J = 3-2$; panel (b): $\text{DNC } J = 3-2$; panel (c): $\text{DCO}^+ J = 3-2$; and panel (d): $\text{HCO}^+ J = 3-2$.

rather compact. Therefore, the effect of missing flux should be small.

The DCO^+ line profile toward the starless sub-core G211D (Figure 17(c)) shows a signature of the inverse P Cygni profile. The absorption feature ($v_{\text{LSR}} = 3.695 \pm 0.035 \text{ km s}^{-1}$ through Gaussian fitting) is redshifted with respect to the radial velocity of the core ($v_{\text{LSR}} = 3.186 \pm 0.006 \text{ km s}^{-1}$) by $0.509 \pm 0.036 \text{ km s}^{-1}$. It is possible that the inverse P Cygni profile represents infall motions, which means that this sub-core is still at the stage of mass accretion. The dust continuum radius $R_{\text{dust}} < 0.002 \text{ pc}$ and the DCO^+ line width $\Delta v (\text{DCO}^+) = 0.29 \text{ km s}^{-1}$ provide a timescale of $< 7 \times 10^3 \text{ yr}$. This value and the dust continuum mass $M_{\text{dust}} = 0.009 \mathcal{M}_{\odot}^{\text{N}}$ lead to a mass accretion rate of $> 1.3 \times 10^{-6} \mathcal{M}_{\odot}^{\text{N}} \text{ yr}^{-1}$. The dip velocity of $\sim 3.8 \text{ km s}^{-1}$ in the DCO^+ profile is appreciably different from that in HCO^+ of $\sim 3.0 \text{ km s}^{-1}$, which is probably due to the missing flux. On the other hand, the velocities in the N_2D^+ and DNC emission are $\sim 3.0 \text{ km s}^{-1}$. It is possible that

the inverse P Cygni profile cannot be explained in terms of missing flux but represents infall motion. Contreras et al. (2018) also reported infall motions toward a pre-stellar core in anIRDC.

5. Summary

We mapped two molecular cloud cores, G210 and G211, in the Orion A cloud with the ALMA 7 m Array and with the Nobeyama 45 m radio telescope. They are bright N_2D^+ cores selected from single-pointing observations with the Nobeyama 45 m radio telescope and are thought to be relatively close to the onset of star formation. G210 is a star-forming core and G211 is starless. These cores show line widths of 0.41 and 0.45 km s^{-1} in N_2D^+ in single-dish observations with the Nobeyama 45 m telescope. Both cores were detected with ALMA ACA 7 m Array in the continuum and molecular lines at Band 6. The star-forming core G210 shows an interesting spatial feature of N_2D^+ : two N_2D^+ peaks with similar

intensities and radial velocities are located symmetrically around the dust continuum peak. One interpretation is that the two N_2D^+ peaks represent an edge-on pseudo-disk, which has little-to-no detectable rotation. The starless core G211 shows a very clumpy substructure and contains multiple sub-cores, which show appreciable chemical differences. The sub-cores in G211 have internal motions that are almost purely thermal. The starless sub-core G211D, in particular, shows a hint of the inverse P Cygni profile, suggesting infall motion.

This paper makes use of the following ALMA data: ADS/JAO.ALMA#2016.2.00058.S. ALMA is a partnership of ESO (representing its member states), NSF (USA) and NINS (Japan), together with NRC (Canada), MOST and ASIAA (Taiwan), and KASI (Republic of Korea), in cooperation with the Republic of Chile. The Joint ALMA Observatory is operated by ESO, AUI/NRAO, and NAOJ. Data analysis was carried out on the open use data analysis computer system at the Astronomy Data Center, ADC, of the National Astronomical Observatory of Japan. Some data were retrieved from the JVO portal³² operated by ADC/NAOJ. K.T. thanks Satoshi Yamamoto and Nami Sakai for discussion. S.O. was partially supported by a Grant-in-Aid for Scientific Research (KAKENHI No. 18K13595) of Japan Society for the Promotion of Science (JSPS). P.S. was partially supported by a Grant-in-Aid for Scientific Research (KAKENHI No. 18H01259) of Japan Society for the Promotion of Science (JSPS).

Facilities: ALMA, No:45m.

Software: AIPS (van Moorsel et al. 1996), CASA (v4.7.2 and v5.4.0; McMullin et al. 2007), NewStar, NoStar, RADEX (van der Tak et al. 2007).

ORCID iDs

Ken'ichi Tatematsu  <https://orcid.org/0000-0002-8149-8546>
 Tie Liu  <https://orcid.org/0000-0002-5286-2564>
 Gwanjeong Kim  <https://orcid.org/0000-0003-2011-8172>
 Jeong-Eun Lee  <https://orcid.org/0000-0003-3119-2087>
 Naomi Hirano  <https://orcid.org/0000-0001-9304-7884>
 Sheng-Yuan Liu  <https://orcid.org/0000-0003-4603-7119>
 Satoshi Ohashi  <https://orcid.org/0000-0002-9661-7958>
 Patricio Sanhueza  <https://orcid.org/0000-0002-7125-7685>
 Neal J. Evans II  <https://orcid.org/0000-0001-5175-1777>
 Gary A. Fuller  <https://orcid.org/0000-0001-8509-1818>
 Miju Kang  <https://orcid.org/0000-0002-5016-050X>
 Siyi Feng  <https://orcid.org/0000-0002-4707-8409>
 Tomoya Hirota  <https://orcid.org/0000-0003-1659-095X>
 Xing Lu  <https://orcid.org/0000-0003-2619-9305>
 Di Li  <https://orcid.org/0000-0003-3010-7661>
 Kee-Tae Kim  <https://orcid.org/0000-0003-2412-7092>
 Ke Wang  <https://orcid.org/0000-0002-7237-3856>
 Mika Juvela  <https://orcid.org/0000-0002-5809-4834>
 L. Viktor Tóth  <https://orcid.org/0000-0002-5310-4212>

References

Aikawa, Y., Furuya, K., Hincelin, U., & Herbst, E. 2018, *ApJ*, 855, 119
 Asayama, S., & Nakajima, T. 2013, *PASP*, 125, 213
 Aso, Y., Tatematsu, K., Sekimoto, Y., et al. 2000, *ApJS*, 131, 465
 Bergin, E. A., Alves, J., Huard, T. L., & Tafalla, M. 2002, *ApJL*, 570, L101
 Blitz, L. 1990, in ASP Conf. Ser. 12, *The Evolution of the Interstellar Medium*, ed. L. Blitz (San Francisco, CA: ASP), 273

Carey, S. J., Feldman, P. A., Redman, R. O., et al. 2000, *ApJL*, 543, L157
 Caselli, P., Pineda, J. E., Zhao, B., et al. 2019, *ApJ*, 874, 89
 Chen, H., Myers, P. C., Ladd, E. F., & Wood, D. O. S. 1995, *ApJ*, 445, 377
 Chen, H.-R. V., Zhang, Q., Wright, M. C. H., et al. 2019, *ApJ*, 875, 24
 Contreras, Y., Sanhueza, P., Jackson, J. M., et al. 2018, *ApJ*, 861, 14
 Crapsi, A., Caselli, P., Walmsley, C. M., et al. 2005, *ApJ*, 619, 379
 Crutcher, R. M. 2012, *ARA&A*, 50, 29
 De Simone, M., Fontani, F., Codella, C., et al. 2018, *MNRAS*, 476, 1982
 Emprechtinger, M., Wiedner, M. C., Simon, R., et al. 2009, *A&A*, 496, 731
 Faure, A., Varambhia, H. N., Stoecklin, T., & Tennyson, J. 2007, *MNRAS*, 382, 840
 Feng, S., Beuther, H., Zhang, Q., et al. 2016, *A&A*, 592, 21
 Fontani, F., Caselli, P., Crapsi, A., et al. 2006, *A&A*, 460, 709
 Fuller, G. A., & Myers, P. C. 1992, *ApJ*, 384, 523
 Furlan, E., Fischer, W. J., Ali, B., et al. 2016, *ApJS*, 224, 5
 Gerner, T., Shirley, Y. L., Beuther, H., et al. 2015, *A&A*, 579, 80
 Getman, K. V., Feigelson, E. D., Kuhn, M. A., & Garmire, G. P. 2019, *MNRAS*, 487, 2977
 Heyer, M., Krawczyk, C., Duval, J., & Jackson, J. J. 2009, *ApJ*, 699, 1092
 Iguchi, S., Morita, K.-I., Sugimoto, M., et al. 2009, *PASJ*, 61, 1
 Kamazaki, T., Okumura, S. K., Chikada, Y., et al. 2012, *PASJ*, 64, 29
 Kauffmann, J., Pillai, T., & Goldsmith, P. F. 2013, *ApJ*, 779, 185
 Kim, G., Tatematsu, K., Liu, T., et al. 2020, *ApJS*, submitted
 Kong, S., Tan, J. C., Caselli, P., et al. 2017, *ApJ*, 834, 193
 Liu, T., Kim, K.-T., Juvela, M., et al. 2018, *ApJS*, 234, 28
 Lombardi, M., Bouy, H., Alves, J., & Lada, C. J. 2014, *A&A*, 566, A45
 Looney, L. W., Tobin, J. J., & Kwon, W. 2007, *ApJL*, 670, L131
 Lu, X., Zhang, Q., Liu, H. B., et al. 2018, *ApJ*, 855, 9
 Lynds, B. T. 1962, *ApJS*, 7, 1
 MacLaren, I., Richardson, K. M., & Wolfendale, A. W. 1988, *ApJ*, 333, 821
 Maddalena, R. J., Morris, M., Moscovitz, J., et al. 1986, *ApJ*, 303, 375
 McMullin, J. P., Waters, B., Schiebel, D., Young, W., & Golap, K. 2007, in ASP Conf. Ser. 376, *Astronomical Data Analysis Software and Systems XVI*, ed. R. A. Shaw, F. Hill, & D. J. Bell (San Francisco, CA: ASP), 127
 Minamidani, T., Nishimura, A., Miyamoto, Y., et al. 2016, *Proc. SPIE*, 9914, 99141Z
 Murillo, N. M., van Dishoeck, E. F., van der Wiel, M. H. D., et al. 2018, *A&A*, 617, A120
 Myers, P. C., Linke, R. A., & Benson, P. J. 1983, *ApJ*, 264, 517
 Nagahama, T., Mizuno, A., Ogawa, H., & Fukui, Y. 1998, *AJ*, 116, 336
 Nakajima, T., Kimura, K., Nishimura, A., et al. 2013, *PASP*, 125, 252
 Nakamura, F., Ishii, S., Dobashi, K., et al. 2019, *PASJ*, 71, S3
 Nakano, T. 1998, *ApJ*, 494, 587
 Ohashi, N., Hayashi, M., Ho, P. T. P., et al. *ApJ*, 488, 317
 Ohashi, S., Sanhueza, P., Sakai, N., et al. 2018, *ApJ*, 856, 147
 Onishi, T., Mizuno, A., Kawamura, A., Tachihara, K., & Fukui, Y. 2002, *ApJ*, 575, 950
 Ossenkopf, V., & Henning, Th. 1994, *A&A*, 291, 943
 Pagani, L., Bacmann, A., Cabrit, S., & Vastel, C. 2007, *A&A*, 467, 719
 Pérault, M., Omont, A., Simon, G., et al. 1996, *A&A*, 315, 165
 Pickett, H. M., Poynter, R. L., Cohen, E. A., et al. 1998, *JQRST*, 60, 883
 Planck Collaboration XXIII 2011, *A&A*, 536, A23
 Planck Collaboration XXVIII 2016, *A&A*, 594, A28
 Poidevin, F., Bastien, P., & Mathews, B. C. 2010, *ApJ*, 716, 893
 Puanova, A., Caselli, P., Pineda, J. E., et al. 2018, *A&A*, 617, A27
 Redaelli, E., Bizzocchi, L., Caselli, P., et al. 2019, *A&A*, 629, A15
 Riaz, B., Machida, M. N., & Stamatellos, D. 2019, *MNRAS*, 486, 4114
 Sakai, N., Sakai, T., Hirota, T., et al. 2014, *Natur*, 507, 78
 Sakai, T., Sakai, N., Furuya, K., et al. 2012, *ApJ*, 747, 140
 Salinas, V. N., Hogerheijde, M. R., Mathews, G. S., et al. 2017, *A&A*, 606, A125
 Sanhueza, P., Contreras, Y., Benjamin, W., et al. 2019, *ApJ*, 886, 102
 Sanhueza, P., Jackson, J. M., Foster, J. B., et al. 2012, *ApJ*, 756, 60
 Savage, C., Apponi, A. J., Ziurys, L. M., & Wyckoff, S. 2002, *ApJ*, 578, 211
 Sawada, T., Ikeda, N., Sunada, K., et al. 2008, *PASJ*, 60, 445
 Soler, J. D., Bracco, A., & Pon, A. 2018, *A&A*, 609, 3
 Stephens, I. W., Dunham, M. M., Myers, P. C., et al. 2018, *ApJS*, 237, 22
 Tafalla, M., Mardones, D., Myers, P. C., et al. 1998, *ApJ*, 504, 900
 Tatematsu, K., Hirota, T., Ohashi, S., et al. 2014, *ApJ*, 789, 83
 Tatematsu, K., Kandori, R., Umemoto, T., & Sekimoto, Y. 2008, *PASJ*, 60, 407
 Tatematsu, K., Liu, T., Ohashi, S., et al. 2017, *ApJS*, 228, 12
 Tatematsu, K., Ohashi, S., Sanhueza, P., et al. 2016, *PASJ*, 68, 24

³² <http://jvo.nao.ac.jp/portal/>

- Tatematsu, K., Umemoto, T., Heyer, M. H., et al. 1998, [ApJS](#), **118**, 517
- Tatematsu, K., Umemoto, T., Kameya, O., et al. 1993, [ApJ](#), **404**, 643
- Tatematsu, K., Umemoto, T., Kandori, R., & Sekimoto, Y. 2004, [ApJ](#), **606**, 333
- Tobin, J. J., Bourke, T. L., Mader, S., et al. 2019, [ApJ](#), **870**, 81
- Tokuda, K., Tachihara, K., Saigo, K., et al. 2019, [PASJ](#), **71**, 73
- van der Tak, F. F. S., Black, J. H., Schöier, F. L., Jansen, D. J., & van Dishoeck, E. F. 2007, [A&A](#), **468**, 627
- van der Tak, F. F. S., Müller, H. S. P., Harding, M. E., & Gauss, J. 2009, [A&A](#), **507**, 347
- van Moorsel, G., Kembell, A., & Greisen, E. 1996, in A.S.P. Conf. Ser. 101, *Astronomical Data Analysis Software and Systems V*, ed. G. H. Jacoby & J. Barnes (San Francisco, CA: ASP), 37
- van 't Hoff, M. L. R., Tobin, J. J., Harsono, D., & van Dishoeck, E. F. 2018, [A&A](#), **615**, A83
- Yi, H.-W., Lee, J.-E., Liu, T., et al. 2018, [ApJS](#), **236**, 51